5-2012

A COMPUTATIONAL PIPELINE FOR MCI DETECTION FROM HETEROGENEOUS BRAIN IMAGES

Lin Li
Clemson University, lindalee.linlin@gmail.com

Follow this and additional works at: https://tigerprints.clemson.edu/all_dissertations

Part of the Computer Sciences Commons

A COMPUTATIONAL PIPELINE FOR MCI DETECTION
FROM HETEROGENEOUS BRAIN IMAGES

A Dissertation
Presented to
the Graduate School of
Clemson University

In Partial Fulfillment
of the Requirements for the Degree
Doctor of Philosophy
Computer Science

by
Lin Li
May 2012

Accepted by:
Dr. Zijun Wang, Committee Chair
Dr. Pradip K. Srimani
Dr. Feng Luo
Dr. Roy P. Pargas

Abstract

The aging population has increased the importance of identifying and understanding mild cognitive impairment (MCI), particularly given that 6 – 15 % of MCI cases convert to Alzheimer's disease (AD) each year. The early identification of MCI has the potential for timely therapeutic interventions that would limit the advancement of MCI to AD. However, it is difficult to identify MCI-related pathology based on visual inspection because these changes in brain morphology are subtle and spatially distributed. Therefore, reliable and automated methods to identify subtle changes in morphological characteristics of MCI would aid in the identification and understanding of MCI. Meanwhile, usability becomes a major limitation in the development of clinically applicable classifiers. Furthermore, subject privacy is an additional issue in the usage of human brain images.

To address the critical need, a complete computer aided diagnosis (CAD) system for automated detection of MCI from heterogeneous brain images is developed. This system provides functions for image processing, classification of MCI subjects from

control, visualization of affected regions of interest (ROIs), data sharing among different

research sites, and knowledge sharing through image annotation.

Dedication

This work is dedicated to my parents. Their love, encouragement, and support have inspired me to complete my dissertation.

Acknowledgments

I would like to thank my advisor, Dr. Zijun Wang. I appreciate all of the guidance, encouragement, support, and help that he provided on my way towards the Ph.D. degree.

I thank Dr. Pradip K. Srimani for serving on my committee and his advice, patience, and encouragement.

I express my appreciation to the other members of my committee, Dr. Feng Luo and Dr. Roy P. Pargas, for reading this dissertation and for their advice during my Ph.D. study.

I would like to thank Dr. Mark Eckert in Medical University of South Carolina for his valuable guidance and suggestions on my research.

Finally, I thank Dr. Zhidian Du, Liang Dong, Dr. Dheeraj Chahal, and Carl Lozar for all of the assistance they provided.

Table of Contents

List of Tables

List of Figures

x

Chapter 1

Introduction

1.1. Motivation

Mild cognitive impairment (MCI) is the transitional phase between normal forgetfulness because of aging and the development of dementia [71]. This can appear in elderly persons from the age of 60 to 65 years. MCI subjects do not have serious problems in their daily lives, but their memory and cognitive functions are problematic. According to the study of dementia in [22], "symptoms of MCI include: taking longer to perform more difficult mental activities, having difficulty performing more than one task at a time", etc.

Our aging population has increased the importance of identifying and understanding MCI, particularly given that 6 – 15 % of MCI cases convert to Alzheimer's

disease (AD) each year [70]. Although no cure for MCI exists, effective treatments like several medications and non-medication approaches may potentially control or alleviate the symptoms. Therefore, in our work [52], we pointed out that it is very helpful to perform early detection of MCI so as to provide a time window to delay or prevent the progression of AD. Biomarkers that reflect the changes in brain tissues have important clinical relevance because they influence treatment plans, such as deciding if an individual with suspected MCI should receive medication or surgical planning [73]. However, it is difficult to identify MCI-related pathology based on visual inspection for the reason that these changes in brain morphology are subtle and spatially distributed [14, 46, 69]. Not every subject exhibits all of the symptoms of MCI, and some other health issues may also contribute to memory loss. Furthermore, no particular test has been designed for the purpose of diagnosing MCI [62]. Additionally, the memory problems slowly and gradually appear, and people usually think that the memory loss is normal because of aging rather than a possible disease [62].

Due to the limitations above, it requires a large amount of clinical judgments to diagnose MCI [35]. Doctors may review subjects' health records and medications, test subjects' cognitive abilities, and perform clinical observations or brain imaging, etc. Evidences suggest that structural magnetic resonance imaging (MRI) can show deterioration of brain tissue in subjects suffering from MCI to AD [88]. Therefore, the study on detection of MCI via analysis of MRI is meaningful and promising. Reliable, automated and non-invasive methods to identify subtle changes in morphological characteristics of MRI would aid in the identification and understanding of MCI.

1.2.   Dissertation Overview

In this work, we present a complete computer aided diagnosis (CAD) system for early and automated detection of MCI from heterogeneous brain images. This system provides functions for image processing, classification of MCI subjects from control, visualization of affected regions of interest (ROIs), data sharing among different research sites, and knowledge sharing through image annotation.

We have accomplished the objective of this work by pursuing the following three specific aims.

(1) Pattern classification. Develop algorithms to locate ROIs that are able to reflect the brain tissue damage in MCI subjects. Look for image features in the selected ROIs that have the best performance in discriminating MCI from control subjects. Pick one behavioral estimate or a combination of behavioral estimates to evaluate the idea of coupling imaging data and behavioral/demographic data for determination of MCI. Evaluate the algorithms by clinical study and machine learning experiments.

(2) Image de-identification. Develop methods to de-identify human brain images for protection of subject privacy. This includes the anonymization of subject-related private information and de-facing of facial features (i.e. nose, eyes, and mouth).

(3) Integrate the classifier trained by our approach for MCI classification and the image de-identification method into a CAD system. In the meantime, functions for image processing, visualization and annotation are implemented in the CAD system as well.

This research is expected to significantly contribute to early and automated identification of MCI, which in turn reduces the occurrence chance of AD. The CAD

system is expected to help clinicians focus on the disease detection, without necessity of writing computer scripts or running computer programs for the brain image analysis that clinicians probably are not very familiar with. To the best of our knowledge, the CAD system will be the first one to provide clinical capability for automated detection of MCI. The image classification function of the system is based on our approach for MCI detection. This method is expected to achieve a high classification accuracy that is comparable to the state-of-the-art methods. The approach is innovative for two reasons. 1) T-value from voxel-wise statistics has been used in the image segmentation. 2) The effect of clinical features on the classification performance has been considered in the study. Because of the privacy issue in Health Insurance Portability and Accountability Act of 1996 (HIPAA), human brain image de-identification is a preliminary requirement for brain imaging study. Therefore, in this work, we propose a de-identification algorithm and integrate it in the CAD system for the purpose of protecting subject privacy and data sharing among different research sites. The image de-identification function of the CAD system is expected to re-label the private information of each subject's data with an unlinked random ID number, and crop out the facial features to obscure the face. Users of our CAD system can use the de-identification function to de-identify the image scans of their research sites on their own computers before uploading them to our system for MCI diagnosis.

1.3.   Dissertation Organization

The rest of this dissertation is structured as follows. Chapter 2 provides a review of background and related work. Chapter 3 gives an overview of the CAD system that we

propose in the work. Chapter 4 describes the image processing function in the CAD system, and this chapter also elaborates the image processing steps that are preliminary and mandatory ahead of the stage of image analysis. In Chapter 5, we discuss the details of our method with statistical analysis and pattern classification for detection of MCI, and discuss its integration into the CAD system. Chapter 6 describes data sharing, knowledge sharing, and other functions (e.g. visualization, data storage, and data retrieval) of the CAD system. We finally conclude our work and list the future work in Chapter 7.

Chapter 2

Background

2.1.   MRI Tools with Diagnostic Capabilities

Image analysis methods that are based on pattern classification usually involve several operations, each of which requires the preparation and execution of computer scripts on MRI data sets. Therefore, clinicians may require a computer expert to help write computer programs and perform the image classification. However, the costs and difficulty finding a qualified computer expert would be prohibitive for a clinical facility. To facilitate the diagnosis and reduce the cost, a CAD system that can automatically process and analyze images for the purpose of disease detection is strongly expected. With the system, clinicians do not need to spend too much time on learning and writing computer scripts/programs, and therefore they can focus on the work in their knowledge

domain. Nevertheless, clinicians may also have problems with installing and configuring a CAD system on their own computers because of the lack of computer knowledge. Hence, an online CAD system that can be shared among clinicians is a reasonable solution to facilitate clinicians to do disease diagnosis. By using the online system, clinicians do not need to worry about how to install and how to configure the software. Instead, they can simply upload a subject's MRI images and conduct the disease diagnosis via the Web interface of the CAD system.

Currently, there are a few MRI-CAD systems used by physicians and researchers. CADstream [12] is originally a CAD system for MRI of the breast. It is now extended with customized applications to satisfy customer's requirements, including applications for breast, liver and prostate MRI. CADstream provides multiple functions, such as automated analysis, 2D/3D motion correction, diffusion analysis, etc. Similarly, the use of Z3D software provides abilities to visualize and evaluate breast lesions by MRI, which improves lesion detection and provides morphological details like speculation and intra-lesion kinetic information [50]. Syngo BRACE [79] – an MRI soft tissue motion correction software, is also a CAD system for MRI of the breast. It is used to remove motion artifacts for the purpose of more accurate diagnosis [79]. iCAD, Inc., provides SpectraLook with CADvue [41] as MRI CAD analysis solutions to "improve the analysis workflow, interventional planning and reporting of breast MR results" [17]. Another solution that includes VividLook analytical power with CADvue [42] is provided for prostate MRI analysis. In a word, the use of CAD systems with MRI significantly

improves the performance of classifying lesions on MRI. However, to our knowledge, there is no CAD system available for detection of MCI.

The research that is related to clinically applicable disease diagnosis from brain images usually involves construction of brain image databases and development of brain image processing and analysis tools. Currently, as pointed out in our work [53], there are a few online brain image databases for public access. For instance, Open Access Series of Imaging Studies (OASIS) [58] is a series of MRI data sets that are publicly available for brain imaging study. The Whole Brain Atlas is a resource of information collected by Harvard medical school "for central nervous system imaging which associates clinical information with magnetic resonance (MR), x-ray computed tomography (CT), and nuclear medicine images" [85]. However, most of these image databases are designed for storage, retrieval or visualization of brain images. They do not provide any abilities to process or diagnose images. On the other hand, many brain image processing and analysis tools lack the associated databases for storage and retrieval of clinical and analysis information. For example, Stroketool is a tool "for calculation and visualization of perfusion- and diffusion-weighted MRI data sets in medical science" [81]. BrainStorm [9] is a toolkit for processing and visualizing Magnetoencephalography (MEG) and Electroencephalography (EEG) data. Without a database on the backend, clinical information cannot be effectively associated with the image processing results for automated disease diagnosis.

Therefore, it is desired to combine brain image processing and diagnosis functions with brain image database system. A few recent projects tried to address this issue.

BrainMaps.org is "an interactive high-resolution digital brain atlas for querying and retrieving data about brain structures and functions" [61]. It provides a suite of desktop applications for users to analyze image data in its database. However, no application can be used to diagnose MCI. Moreover, those applications need to be individually installed on each user's computer, which must satisfy a certain minimum system requirements. It is inconvenient for a clinician or a technician who probably lack necessary computing skills to install and configure such applications. The team of M.R. Siadat presents a human brain image database system [77, 78] which has a bunch of image processing and query tools integrated and can be used for management, navigation, and retrieval of medical images. However, this system is for Epilepsy detection only, and it does not include an image annotation tool through which users can annotate on certain regions of the brain image to assist clinical diagnosis.

To sum, the systems that are mentioned above are either for data query only or for image processing or visualization only. Or some of them are desktop applications, which are difficult for clinicians to install and maintain. Additionally, these applications do not have a common database shared among different users so that data sharing and knowledge sharing can be achieved. Most importantly, no application is available for MCI detection. To address these issues, in this work, we propose an online automated system that provides users the ability to process, analyze, visualize and annotate image data for the purpose of MCI detection. This online CAD system addresses the challenge to implement CAD systems at specific medical institutions. Maintaining a CAD system for each medical institution may not be practical because of the considerable computing

9

cost that is necessary to develop and maintain the computing environment, and to process and diagnose brain images.

2.2.   Methodologies for Classification of MCI

The medial temporal lobe is particularly affected in people with MCI and AD [28, 5, 21, 83, 86, 11]. Volumetric MRI measures of the hippocampus and entorhinal cortex have been used to classify MCI cases from controls [5, 90]. However, the volume measurement of certain brain structures cannot represent the widespread pattern of brain atrophy in people with MCI, compared with voxel-based measures [30, 69, 84, 15, 39, 6, 38, 87]. Since the brain atrophy in MCI is complex, subtle, and may be distributed over several regions or within portions of specific regions [14], operators may not be able to trace all of the atrophic regions. Some atrophic brain regions in MCI subjects may be overlooked, thereby limiting classification accuracy. Moreover, specific brain regions have to be outlined manually, which is time-consuming and not easily reproducible across operators. Recently, some studies [16, 23] have tried to solve this issue by using software to segment brain regions as an alternative to manual tracing. The study [10] has also proposed a fully automated approach for volumetric MRI acquisition to overcome several hurdles (e.g. "a lack of standardized MRI acquisition protocols" [10]) of its application in clinical practice. However, experiments [90, 48] have showed that volumetric measures appear more effective at predicting severe cases of AD than MCI. This is reasonable because the regional progression of neuropathology that results in

10

atrophy of affected structures in patients with AD is well structured [7] and can be detected with volumetric MRI measures [20].

Compared with volumetric MRI measures for the measurement of large regions, voxel based morphometry (VBM) [2] is able to investigate minor focal differences across brains. VBM analysis provides the opportunity to identify important disease features from across the brain and can easily be replicated across sites in a short amount of time. The voxel-by-voxel measurement involves a voxel-wise comparison of the brain tissue over the whole brain between MRI scans of patients and healthy controls. Most recent studies [69, 84, 15, 39, 6, 38, 87] have used this method for two reasons. (1) The method can identify all the brain regions that demonstrate significant tissue loss. Hence, it is not biased to specific brain structures and can give an unbiased assessment of structural differences throughout the brain [2]. (2) It does not need the delineation of specific brain regions, which therefore saves time and reduces the possibility of operator dependent errors. These studies [69, 84, 15, 39, 6, 38, 87] have found the patterns of brain atrophy in MCI, which mainly involve medial temporal lobe structures. Voxel-based measures of brain atrophy have provided modestly higher classification accuracy for MCI than gross volumetric measures [84, 39]. For example, 87% of early AD cases and controls were successfully classified using Z-score values from voxels within medial temporal lobe regions [39].

Voxel-based analyses have been useful in providing greater classification accuracy, particularly when coupled with machine learning classifiers and pattern classification techniques [19, 31, 30, 49, 63]. Studies [69, 84, 15, 39, 6, 38, 87] using

only voxel-based analyses always use the brain regions (e.g. thalamus, hippocampus, etc.) that are already known beforehand. These researches study the gray matter (GM)/white matter (WM) intensity differences in those regions between MCI cases and controls to confirm the tissue loss in the regions. Or they use the intensity differences (usually z-score) in the well-known brain regions for classification of MCI [39]. Since the atrophy in patients of MCI may not exactly occur in certain pre-known brain regions, it may be more helpful to dynamically find the atrophic regions – regions of interest (ROIs), based on intensity differences of GM or WM, so as to determine the atrophic pattern of MCI subjects. By applying pattern classification techniques coupled with voxel-based analyses, some studies have already achieved impressive accuracy for classification of MCI. For instance, Klöppel et al. [49] achieved an 88.9% classification accuracy, and Davatzikos et al. [19] claimed a 90% classification accuracy in their respective articles. In [49], GM volumes in the whole brain and medial temporal lobe regions were used as the features for classification. However, taking the whole brain into consideration without differentiating atrophic regions from normal regions may decrease the classification power. Davatzikos's method [19] is better in that it made a selection of atrophic brain regions. Nevertheless, it only used 15 controls and 15 MCI subjects for experiment. The small sample set may lead to an unreliable result that cannot be generalized to new data sets. Meanwhile, usability is another limitation of the classifier in Davatzikos's method.

12

2.3.   Image Segmentation

Image segmentation is very important in image processing, because segmentation accuracy largely determines the results of image analysis. The goal of segmentation is to cluster an image into multiple regions [34]. Generally speaking, image segmentation algorithms are based on properties of intensity values, which are discontinuity and similarity [34]. The approaches that are based on the discontinuity of intensity values are to partition an image according to the sudden changes in intensity, such as points, lines, and edges [67]. On the other hand, the approaches based on similarity of intensity values use certain predefined criteria and the similarity of intensity to partition an image into regions [67]. In addition, there are some other segmentation techniques (e.g. morphological watershed segmentation [60]) that combine segmentation algorithms based on discontinuity or similarity of intensity values [34], and they are able to produce more stable segmentation results.

There are several techniques for detecting discontinuities of intensity values in a digital image. The most common way is to run a mask, which "involves computing the sum of products of the coefficients with the gray levels contained in the region encompassed by the mask" [27]. Compared with point and line detection, edge detection is the most often used approach. In the category of approaches that are based on intensity similarity, thresholding and region growing are more popular. Using a global threshold is the easiest thresholding technique to partition an image. Adaptive thresholding is used in the situation that a fixed global threshold is not enough to effectively partition an image because of factors like uneven illumination [8, 75]. The thresholding can be adaptive

because the threshold of each pixel may be different according to the position of the pixel.

Region growing procedure clusters pixels or small regions into larger regions according to pre-defined criteria [34]. Seeded region growing algorithm is initially proposed in the article [1] by R. Adams and L. Bischof. Later on, many variations [89, 76, 18, 40, 55] of region growing algorithm have been presented to tackle the segmentation problems in different images or applications. The principle of seeded region growing segmentation is to find regions in images by growing regions centered on a bunch of "seed" points. Given a set of seeds, the algorithm starts from one seed, and grows a region around the seed by clustering its neighboring pixels that have properties similar to the seed. Then the algorithm basically repeats the procedure and grows other regions centered on the other seeds.

The hypothesis of our research for MCI classification is that the atrophy occurs in regions rather than standalone voxels. Therefore, we design a region growing algorithm to look for the atrophic regions instead of specific voxels. However, since the atrophic regions are unknown beforehand and are very subtle and may be distributed, it is impossible to pre-determine the "seeds" and then start growing regions from the seeds. To solve the issue, we design an unseeded region growing algorithm coupled with thresholding to determine the ROIs. Moreover, intensity similarity is not used in our region growing algorithm. Instead, t-values produced by voxel-wise statistics are used in the similarity-based search. We have used t-values to grow regions because t-values can reflect the statistical intensity differences of voxels across MCI subjects and control. We

care more about the differences of intensity that can characterize MCI subjects than the intensity itself.

2.4.   Subject Privacy and Image De-identification

Because of the constraint of institutional review board (IRB) protocols, medical research usually cannot get enough data of subjects. Especially in the area of medical imaging, subject related information that could be used to identify a subject is highly protected. In our research, we also face the problem of limited data sets, although the data set that we use is larger than the other research in the same area. To increase the number of experimental data in our research, we would like to collect the brain images that are uploaded to the CAD system. These brain images from more people, more races and regions will be added to our current experimental data sets for building a more robust and reliable model so as to further improve the classification accuracy. We also encourage data sharing among various research sites to allow researchers collaboratively share image data of their research sites to contribute to the diagnosis of disease. The first problem that needs to be addressed for sharing human brain images is how to ensure that there will be no HIPAA violations and that image data can be appropriately de-identified. IRBs consider random identification numbers and the faces within images as information that could identify a subject. This means that each subject's data needs to be relabeled with an unlinked random ID number and the facial features need to be cropped out or altered to obscure the face. With regard of our system, the first kind of image to be de-identified is Digital Imaging and Communications in Medicine (DICOM) image.

DICOM [24] is a standard to store and transmit medical imaging data, which "includes a file format definition and a network communication protocol" [25]. A subject's DICOM image consists of several data items, including the subject's profile information such as name, ID, birthday, etc. For the purpose of sharing DICOM images in multisite projects, it is very important that the usage should abide by HIPAA. HIPAA requires that personal information of individuals who participate in the research must be protected. For this reason, it is essential that DICOM images are anonymized before being transmitted for sharing, which means that a subject's confidential data must be replaced with random strings. On the other hand, one of the HIPAA-defined identifiers that must be removed is "full face photographic images and any comparable images" [82]. Regarding DICOM brain images with facial features (i.e. mouth, nose and eyes), although they are usually presented in 2D slices, a 3D image that explicitly shows a subject's facial features can be easily rendered from 2D slices. This is why a subject's DICOM brain images need to be defaced (e.g. cut out or mask or alter facial features). Through the anonymization and the image defacing, DICOM brain images can be de-identified and safely shared in multisite projects.

With respect to anonymization, consistency is a legitimate requirement. After anonymization, a subject's DICOM images and the profile data in DICOM header files should remain connected. Additionally, a subject's demographic and behavioral data file should be anonymized with the same random string as the one used to anonymize the subject's DICOM images. The link between the images and the image header files as well as the demographic data files keeps the information of the same subject together.

Otherwise, a single subject's information would be broken into unrelated pieces, thereby destroying the relationship between the original images and the header files and the demographic data [72]. As for image defacing, a key requirement for DICOM image defacing process is to keep the brain tissues intact while removing the facial features.

Currently, there are a number of programs for DICOM data anonymization [29, 33]. However, they all have some problems to be addressed. Some tools hide data items by simply replacing them with blank (e.g. null subject ID). Totally blanking the subject ID may cause all subjects having the same null ID and thus probably result in the information of two totally unrelated people mixed together. On the other hand, some tools simply delete private data items from DICOM data for the anonymization purpose. However, deletion of data items may lead to an invalid DICOM format. To avoid destroying the DICOM data format, some programs only allow the anonymization of certain items, such as the patient name. Obviously these programs lack the flexibility for DICOM data anonymization. In contrast, a few programs have made the anonymization flexible, by which users can select data items to be anonymized. However, these programs require users to write scripts using script languages, which may be difficult for clinicians.

Meanwhile, there are also some tools for image defacing. Mbirn [59] is a defacer for structural MRI, however, it requires users to construct models of non-brain structures [4]. There are some other articles [74, 37, 91] on skull stripping, which can cut out the skull and keep the brain tissues. However, skull stripping may be too excessive to be applied in image defacing that only needs to take out facial features. Moreover, currently

17

there is no single tool that provides both anonymization and image defacing functions. Therefore, users have to employ two standalone programs for the purpose of de-identification. Such an approach may result in losing association between images and their related data.

Therefore, to solve the problems with current de-identification tools, it is desirable to develop a DICOM de-identification method for DICOM brain images de-identification. With this method, image defacing does not need the construction of a brain mask or models of non-brain structures, and image anonymization is flexible yet simple. This de-identification method has been integrated in our CAD system.

Chapter 3

Overview of the CAD System

3.1. Introduction

In this work, we have built an online MRI-based CAD system for early and automated detection of MCI. The system is expected to provide image processing, classification, visualization, and annotation functions through which the uploaded patient's MRI scans can be automatically processed and diagnosed. In detail, the CAD system has five features. (1) It is Web-based so that users can use it without the necessity of installing and configuring software. (2) ROIs can be visualized as color map overlays in 2D brain image slices. Users can annotate on certain regions of the brain images. (3) It encourages data sharing and knowledge sharing. Image data in different research sites can be shared as long as users of the data are under IRB protocols and the images are de-

identified. In addition, the system provides collaboration capabilities so that users who have permissions to access the image files can collaboratively visualize and annotate the images. (4) It has a database for storage and retrieval of image data, demographic data, and image analysis results. (5) It provides functions for image processing and disease diagnosis. To the best of our knowledge, the system will be the first one to provide the capability of automated computer aided diagnosis of MCI.

3.2.   System Architecture

The CAD system is composed of three layers: the data access layer, the business logical layer and the presentation layer, as shown in Figure 3.1. The presentation layer is the media between user and the system, recognized as a Web-based user interface. The business logic layer provides the service logic, which is implemented on an Apache Web server. The data access layer that provides data support for the entire system is represented as the data server. The data server stores data and hosts programs to access data in the file system and the database. The major functions that the CAD system provides include: image processing, classification of MCI, data sharing, knowledge sharing, image visualization, and information storage and retrieval. Details of functions are described in the following chapters.
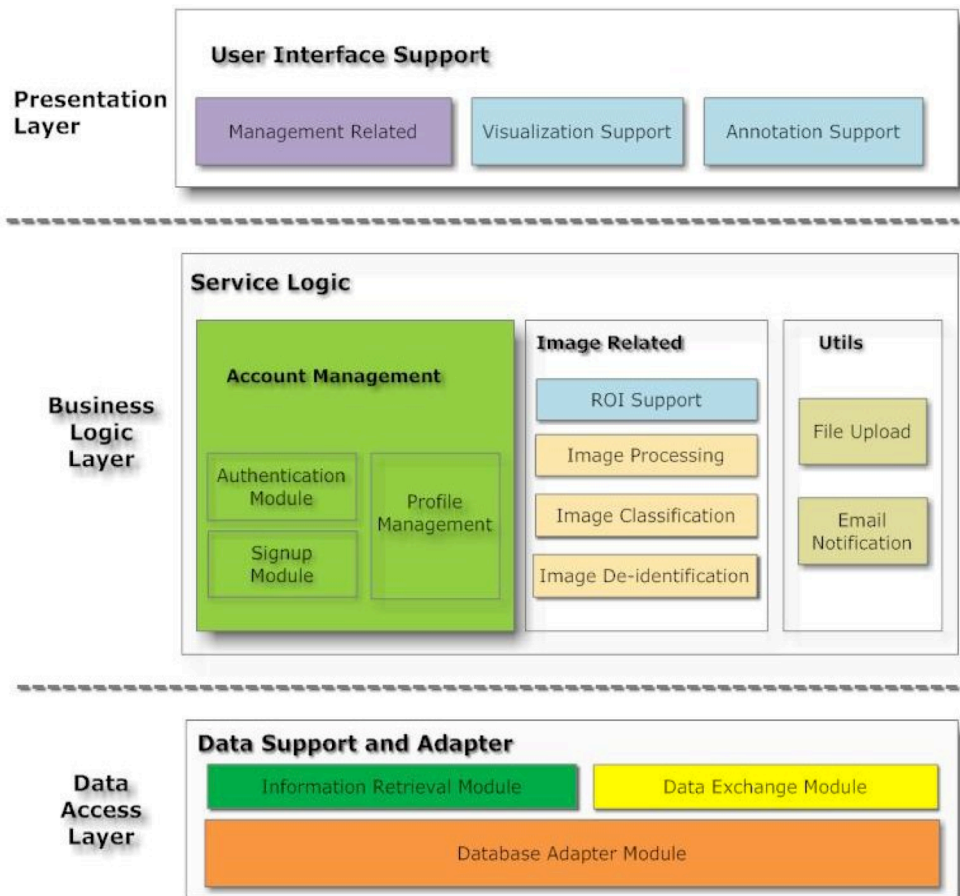
Figure 3.1 The three layers architecture of the CAD system

Chapter 4

Image Processing

4.1.   Introduction

Data used in this work for detection of MCI were selected from the OASIS database [58, 56, 66]. The OASIS images were acquired with a high-resolution T1-weighted 3D magnetization prepared rapid gradient echo (MPRAGE) sequence [65] with a resolution of $1.0 \times 1.0 \times 1.25$ mm^3, TR = 20 ms, TE = 4 ms, flip angle = 10 degrees [58]. For each subject, 3 to 4 scans had been realigned and averaged by the OASIS group. We first segmented and normalized these images and performed bias field correction using an integrated generative model (unified segmentation) [3]. The image processing was conducted with statistical package SPM5 [80]. We then produced GM, WM and cerebrospinal fluid (CSF) study-specific a priori templates by averaging the segmented

22

and normalized images across the MCI and control datasets. After that, the unified

segmentation was performed again for each subject using the study-specific a priori

templates. Modulation was conducted after image normalization. Finally, the segmented,

normalized and modulated images were re-sliced to a 2 mm^3 resolution and smoothed.

Figure 4.1 presents an overview of the image processing in our work. The details

of each processing step are elaborated in the following subsection. The MRI that we take

as an example here is downloaded from OASIS database.
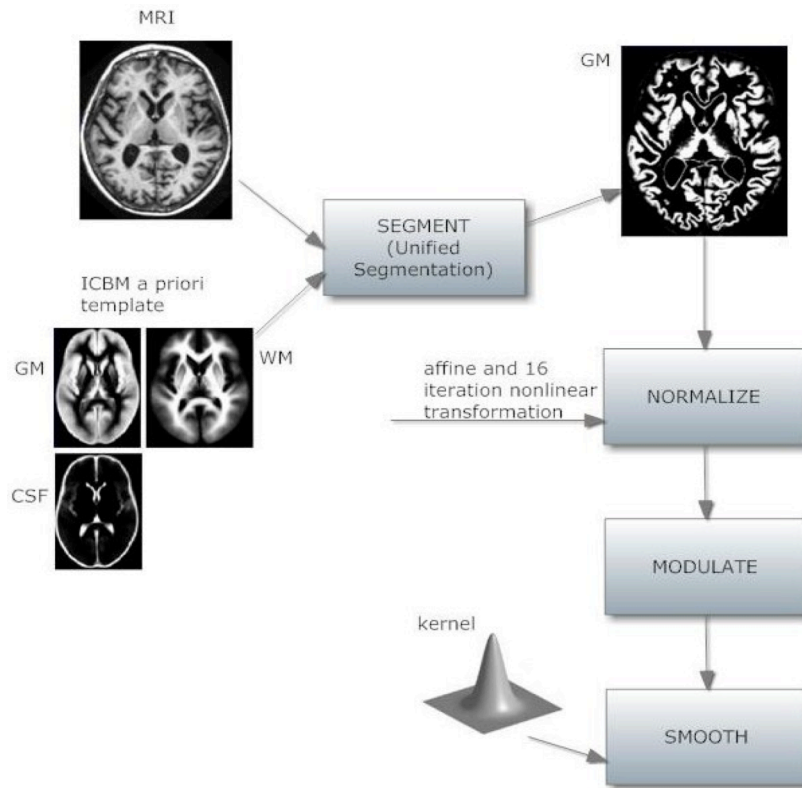
Figure 4.1 The flow chart of image processing in our work.

4.2.   Details of Each Processing Step

In our work, unified segmentation is used to segment brain MRI. Unified segmentation integrates "image registration, tissue classification, and bias correction" [3]. Bias field correction is used to reduce the variation of image signals that may degrade the performance of image segmentation. Tissue classification is based on a mixed Gaussians model. This model reflects the intensity probability density with Gaussian distributions. Rather than assuming prior proportion of voxels in each class of tissue (e.g. gray matter, white matter, CSF, soft tissue, etc.), tissue probability maps (TPMs) of gray matter, white matter and CSF are used as the prior. The template we used in this work is the ICBM Tissue Probabilistic Atlas [43]. In addition, after the first round of segmentation and normalization, in order to segment and normalize the subject images to an age-appropriate template, we performed the unified segmentation again for each subject using the study-specific a priori templates. The output of image segmentation is images with GM, WM and CSF segmented. These segmented images as well as the inverse of affine and 16 iteration non-linear transformations that align the TPMs are input into the image normalization stage.

After image segmentation, image normalization takes the segmented MRI and the inverse of transformations that aligns the TPMs as input, and then transforms MRI of all subjects with different sizes into MNI space. MRIs of all subjects are normalized to a size of $91 \times 109 \times 91$. Because of volume displacement during image normalization, image modulation is required to correct voxel signal intensity. After that, image smoothing is

24

conducted to reduce noise within an image. In our study, a kernel of 10 mm is used in image smoothing to ensure the data are normally distributed.

4.3.   Effect of Image Processing

In order to show the effect of image processing in our work, we compare the output image of each processing step in Figure 4.2. Image 1 in this figure is the original MRI (in ANALYZE format) from OASIS database, with GM, WM and CSF not segmented yet. After segmentation, GM, WM and CSF are segmented to different images. Image 2 presents the GM segment of image 1. We only demonstrate GM segment here because GM is the brain tissue that we have used for image analysis in this work. Compared to image 2, the brain slice in image 3 has a larger size. This is the effect of normalization, which maps images of each subject into one standard space. If the brain of a subject is of comparatively bigger size (i.e. larger than the standard space), then the normalization process will decrease the size to fit in the standard space. The effect of modulation and smoothing is shown in image 4, which is slightly blurred in comparison with image 3.
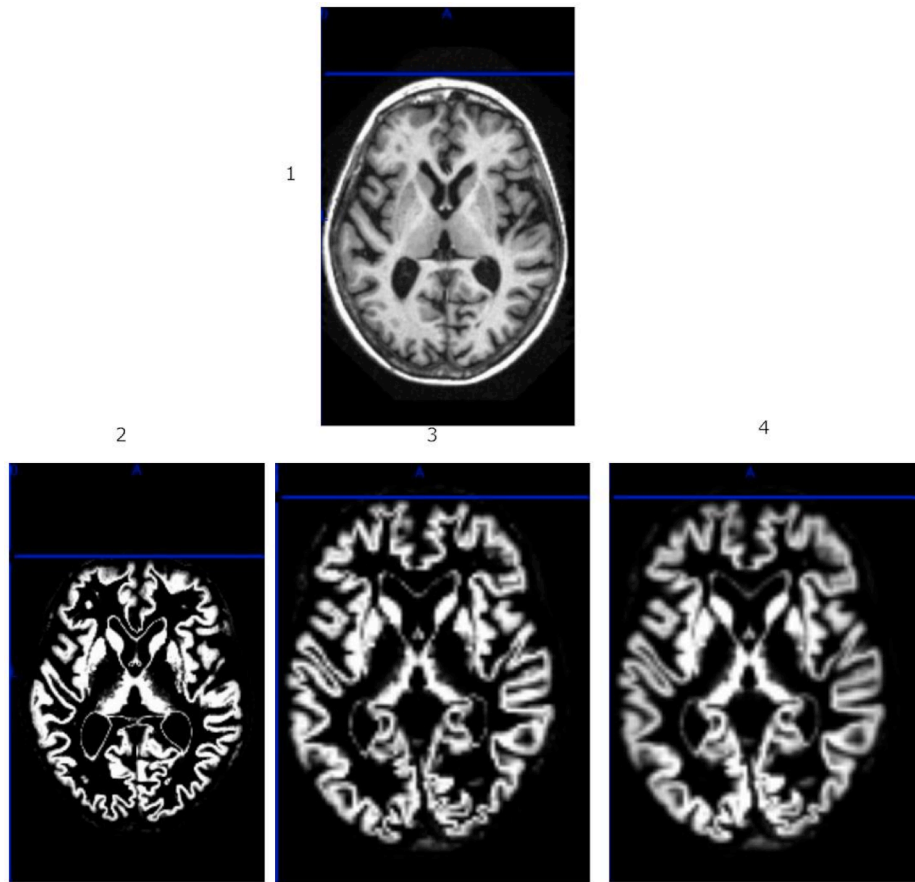
Figure 4.2 The comparison of image output of each image processing step

The image processing steps could possibly affect the analysis results. Skull-stripping, segmentation, and a study-specific template were used to enhance the quality of normalization within the framework of the widely used SPM algorithms. Spatial normalization error with the "unified segmentation" procedure used in this study could have occurred in regions of significant medial temporal atrophy in MCI subjects compared to control subjects. For this reason, it is possible that more recent normalization procedures (e.g. diffeomorphic) would yield superior classification with

better alignment between MCI and control groups. We chose the image processing in this study because they are easily replicated, widely used, and could more easily be implemented in a clinical setting compared to other procedures that would require technical expertise. The modulation procedure could have underestimated group differences in voxel intensities in regions of the hippocampus adjacent to the temporal horn of the lateral ventricle where modulation would increase signal intensity because the ventricle have to be reduced in size to fit to the template. One important point is that the largest source of classification error is related to brain size. Age-cohort and gender specific classification procedures are most likely to yield improvements in classification compared to smaller contributions from improvements in image processing.

4.4.   Function of Image Processing in the CAD System

In our CAD system, users can start processing the uploaded image by simply clicking a button on the Web interface. When a user issues a request to process a subject's image file, the matlab script hssc_cad.m is called for image processing. The flowchart of the script is shown in Figure 4.3. It takes the image file as the input and the output results are listed in Table 4.1. There are three kinds of processing results, gray matter (GM), white matter (WM), and cerebrospinal fluid (CSF) results which filenames are respectively labeled with "c1", "c2" and "c3".
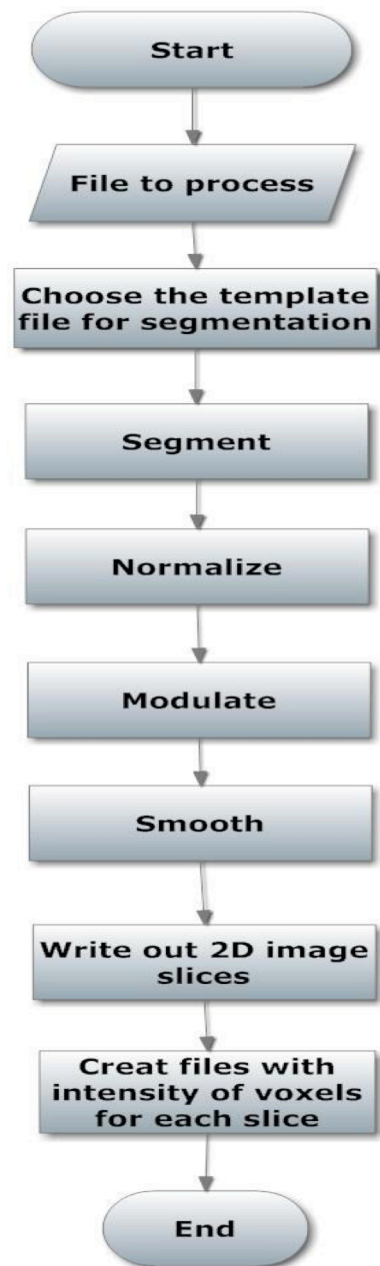
Figure 4.3 The workflow of the script for image processing

Table 4.1 The output of image processing script

Phase	Output
Segment	c1(c2/c3)filename.hdr c1(c2/c3)filename.img
Normalize	wc1(wc2/wc3)filename.hdr wc1(wc2/wc3)filename.img
Modulate	mwc1(mwc2/mwc3)filename.hdr mwc1(mwc2/mwc3)filename.img
Smooth	smwc1(smwc2/smwc3)filename.hdr smwc1(smwc2/smwc3)filename.img
Create 2D image slices	filename(slice#).png
Create intensity file for each slice	filename(slice#).txt

Chapter 5

Detection of MCI

5.1.   Introduction

Early identification of MCI has the potential for timely therapeutic interventions

that would limit the advancement of MCI to AD. The function for classification of MCI

in our CAD system is based on our approach proposed for early detection of MCI

through pattern classification of MRI data. The approach consists of image feature

selection and support vector machine (SVM) classification. Subjects were selected from

the OASIS database and included 89 MCI subjects and 80 controls. Voxel-by-voxel

differences in GM intensity between the MCI and control groups were identified. Then

ROIs and the most discriminative image features that represented the patterns in MCI

subjects were determined for training a classifier. The classifier demonstrated high

classification accuracy (90%) when a behavioral estimate of MCI subjects and the ROIs were included as features, in comparison to the classification accuracy of using the behavioral estimate or the ROIs alone. The classifier has been integrated in our CAD system to provide classification capability of MCI.

5.2.   Participants

The dataset from the OASIS database is collected under the OASIS Data Use Agreement. It consists of 416 participants, aged from 18 to 96, including 100 subjects with very mild to mild cognitive dementia. According to the article [58], "For each subject, 3 or 4 individual T1-weighted MRI scans obtained in single scan sessions are included". Dementia status is characterized using the Clinical Dementia Rating (CDR) [64]. The CDR value of 0 indicates no dementia, and CDR value of 0.5, 1 and 2 represent very mild-, mild-, or moderate-dementia [58]. Mini-mental state examination (MMSE) score is an estimate of the severity of cognitive impairment in an individual, which ranges from 30 (best) to 0 (worst). Compared with the subjects without dementia, the older subjects with dementia have lower MMSE scores [58].

The data set in this study included 89 MCI subjects [55% female, 45% male, mean age = 76.6 (7.3) years] and 80 controls [65% female, 35% male, mean age = 75.2 (8.4) years] (Table 5.1). From the 100 MCI subjects available in the OASIS database, one individual was excluded due to scanner artifacts in the raw images and another subject was excluded because of a potential lesion in lateral occipital cortex. The other 9 participants were excluded due to segmentation error. There were no statistically

significant differences between the groups in gender (χ^2 = 1.73, df = 1, N = 169, 0.10 < P

< 0.20), age (t = 1.18, df = 167, N = 169, two-tailed P = 0.24) or socioeconomic status

(SES) (t = 1.20, df = 167, N = 169, two-tailed P = 0.23). Control subjects were more

likely to have a higher level of education than MCI subjects (t = 2.28, df = 167, N = 169,

two-tailed P = 0.02).

Table 5.1 Demographic and clinical variables of the MCI group and the control group

Group	MCI	Control
No. of subjects	89	80
Female/Male	49/40	52/28
No. of left-handed	0	0
Age, mean [SD]	76.58 [7.28]	75.15 [8.41]
Years of education, mean [SD]	2.82 [1.34]	3.29 [1.33]
SES, mean [SD]	2.69 [1.17]	2.48 [1.10]
MMSE, mean [SD]	24.4 [4.21]	28.9 [1.24]
CDR, mean [SD]	0.70 [0.30]	0 [0]

5.3.   Statistical Analysis and Pattern Classification

Voxel-wise group comparisons were performed using the GM images. This

involved voxel-by-voxel t-test that identified GM intensity differences between the MCI

group and the control group. Given a voxel u of an image, the t-value that measures the

group differences of GM intensity at this voxel is calculated as follows:

$$t(u) = \frac{\text{Avg}(f(u))_1 - \text{Avg}(f(u))_2}{\sqrt{\dfrac{\sigma(f(u))_1^2}{N_1} + \dfrac{\sigma(f(u))_2^2}{N_2}}} \tag{5.1}$$

where $\sigma(f(u))_1^2$ is defined as

$$\sigma(f(u))_1^2 = \frac{\Sigma\left(f_i(u) - \text{Avg}(f(u))_1\right)^2}{N_1} \tag{5.2}$$

and $\sigma(f(u))_2^2$ is defined as

$$\sigma(f(u))_2^2 = \frac{\Sigma\left(f_j(u) - \text{Avg}(f(u))_2\right)^2}{N_2} \tag{5.3}$$

In equation (5.2), i denotes the ith sample in the control group, and $f_i(u)$ is the GM intensity of voxel u in the ith sample. $Avg(f(u))_1$ is the mean of $f_i(u)$ over all samples in the control group, and N_1 is the number of subjects in this group. Similarly, in equation (5.3), j denotes the jth sample in the MCI group, and $f_j(u)$ is the GM intensity of voxel u in the jth sample. $Avg(f(u))_2$ is the mean of $f_j(u)$ over all samples in the MCI group, and N_2 is the number of subjects in this group. T-value of GM intensity at a voxel can reflect the voxel's GM atrophy in a statistical manner. The larger the absolute value of a voxel's t-value is, the more GM atrophy occurs at this voxel.

To find the most discriminative voxels, we calculated t-values of all voxels, a total of 902629 voxels. There were 902629 voxels in each subject's MRI because all the images were scaled to a dimension of $91 \times 109 \times 91$. After computing the t-values of all voxels, we did not use the peak voxels from within affected brain regions (e.g. hippocampus, medial temporal cortex). Instead we applied pattern classification that can globally capture complex relationships in high-dimensional spaces among many brain

regions to most effectively characterize group differences between MCI subjects and control subjects. The idea has the following considerations. First, morphological changes of brain tissues usually occur in regions with irregular shapes, rather than in isolated voxels, and these regions are not known a priori [32]. Second, the voxel with peak t-value within a SPM cluster is locally extracted and thus may not be reliable because of registration errors or noise. In our study, the rules to locate a ROI were: 1) voxels in a ROI should be relevant, which means that voxel coordinates in a ROI had to be continuous in 3D spatial neighborhood. 2) The degree of atrophy in a ROI should be similar. That is to say, t-values of voxels in a ROI had to be all larger than a t-value threshold (explained in the next paragraph) or all smaller than the threshold. This prevents the possibility that only one or very few voxels in a cluster have very high t-values with the rest of voxels in the cluster having much smaller t-values.

To find out the atrophic regions in images of MCI subjects, a threshold-based unseeded region growing algorithm was designed to identify the regions or distributions of voxels affected in MCI subjects. We first sorted voxels (a total of 902629) in a descending order of the absolute values of the corresponding t-values, and then applied the unseeded region growing algorithm. Please note that the absolute value of t-value was used in our entire method. In later sections, when using t-value, we actually mean the absolute value of t-value. The flow chart of the region growing procedure was described in our former work [52], as shown in Figure 5.1.

start

put all the voxels information into a file,
in which each row represents a voxel (the first three columns
are the coordinates x, y and z, the fourth column is the t-value, the fifth column
is a flag that records if the voxel is clustered or not, and the sixth column
is the cluster number which the voxel is in).
The rows are sorted by the descending order of the t-values.

mark each voxel as unclustered

set each voxel's cluster number = -1

set the threshold T of t-value

set the current index of cluster = 0

new a stack

set the center voxel's cluster number = the current index of cluster

mark the center voxel as clustered

take an unclustered voxel that has the largest t-value as the initial center of the new cluster

add the current index of cluster by 1

Are there any unclustered voxels?

Yes

No

end

find the center voxel's unclustered neighboring voxels

Does such neighboring voxel exist?

No

Is the stack empty?

Yes

Yes

No

pop one voxel from the top of the stack and set it as the new center of the current cluster

Do both t-value of the neighboring voxel and t-value of the center voxel >= T OR both of them <=T?

Yes

No

set the neighboring voxel as clustered

set the neighboring voxel's cluster number = the center voxel's cluster number

push this neighboring voxel into stack

Figure 5.1 Region growing procedure. When the procedure ends, every voxel is clustered, and voxels with the same cluster number are in the same region. Regions with more discriminative power are identified earlier.

35

Since we did not have a priori and full knowledge of which brain regions were abnormal, we did not start the region growing procedure with explicit seeds. Instead, the whole brain was searched and the seeds were automatically generated by the region growing procedure. Moreover, the region growing procedure started from the voxels with large t-values so as to make the regions with more discriminative power be identified earlier than the regions with less discriminative power. Also, the region segmentation algorithm segmented the relevant voxels in a ROI, in which the voxels were spatially connected and the t-value were similar. We first observed the distribution of the number of voxels which t-values were in the range of $[0, 1)$, $[1, 2)$, $[2, 3)$, … , and chose the boundary t-value M which satisfied the following condition: the number of voxels which t-values were in the range of $[M, M + 1)$ was dramatically smaller than the number of voxels which t-values were in $[M – 1, M]$. Two boundary t-values ($M = 2$, and $M = 3$) were selected in this step. As we know, changes in brain tissues that reflect the pathological processes of MCI are very subtle to detect. Therefore we made the selection based on the assumption that the number of voxels in atrophic regions, where all voxels have large t-values, should be much smaller than the number of voxels in normal regions where all voxels have small t-values. Among the two boundary t-values, we picked one that resulted in a good segmentation result by using this value as the pre-determined threshold in region segmentation. As there should be multiple regions influenced by MCI, a good segmentation result should get more than one region having voxels with high t-values (i.e. atrophic regions). In our experiment, by using $M = 2$ as the threshold in region segmentation, only one region had all voxels with high t-values while other

36

regions had voxels with much smaller t-values. By using M = 3 as the threshold in region segmentation, voxels with large t-values were not clustered into only one region. Instead, they distributed over several regions. Therefore, we picked M = 3 as the pre-determined threshold for region segmentation. Finally, we fine-tuned the pre-determined threshold (M = 3) by adjusting the threshold to 2.1, 2.2, …, 2.9, 3.1, 3.2, …, 3.9. We used each of the values as the threshold and applied region segmentation and classification, to finally determine the threshold with which the region segmentation result was good and the classification could achieve the highest accuracy. Our experiment showed that using 3.1 as the threshold of t-value can provide a good region segmentation and high classification accuracy.

The unseeded region growing algorithm is based on an idea of "wave transition". That is to say, given three voxels v1, v2 and v3, if v1 and v2 are spatially connected and they have similar t-values, then v1 and v2 are neighbors in the same cluster. If v2 and v3 are also spatially connected and their t-values are similar, then v2 and v3 are neighbors in the same cluster. Therefore, we can infer that v1, v2 and v3 are all neighbors in the same cluster. The statement "two voxels have similar t-values" means the two voxel's t-values are greater than or equal to the threshold of t-value or both of them are smaller than the threshold. Based on the "wave transition", the algorithm starts from using the voxel that has the largest t-value as the center voxel of a cluster, and then looks for all the neighboring voxels of this center voxel. Given a voxel which coordinates are (x, y, z), we look for all its spatially connected voxels, 26 in total. In the same slice as the center voxel, there are 8 adjacent voxels, including (x - 2, y, z), (x + 2, y, z), (x - 2, y - 2, z), (x, y - 2,

z), (x + 2, y - 2, z), (x - 2, y + 2, z), (x, y + 2, z), (x + 2, y + 2, z). Because of the coordinate system of our images, the distance between two adjacent voxels with the same coordinates in two directions is 2 (e.g. voxel (x, y, z), and voxel (x – 2, y, z) are adjacent, with the same values of the y coordinate and the z coordinate). Similarly, in the slice ahead to the slice of the center voxel (i.e. the z coordinate of all voxels in this slice is z - 2), there are 9 adjacent voxels, including (x - 2, y, z - 2), (x, y, z - 2), (x + 2, y, z - 2), (x - 2, y - 2, z - 2), (x, y - 2, z - 2), (x + 2, y - 2, z - 2), (x - 2, y + 2, z - 2), (x, y + 2, z - 2), and (x + 2, y + 2, z - 2). There are other 9 adjacent voxels in the slice that follows the slice of the center voxel (i.e. the z coordinate of all voxels in this slice is z + 2). They are (x - 2, y, z + 2), (x, y, z + 2), (x + 2, y, z + 2), (x - 2, y - 2, z + 2), (x, y - 2, z + 2), (x + 2, y - 2, z + 2), (x - 2, y + 2, z + 2), (x, y + 2, z + 2), and (x + 2, y + 2, z + 2). Our algorithm checks the validity of coordinates of these adjacent voxels (i.e. the coordinate values should not exceed the upper and the lower boundaries of the image). For those adjacent voxels that have valid coordinates, the algorithm selects the voxels which t-values are similar to the center voxel as the center voxel's neighbors. This means that physically connected voxels are not necessarily the neighbors. Then the algorithm takes the neighboring voxels as the new center voxels, and starts growing regions around the new centers. This "looking for neighbors of neighbors" procedure repeats until no more voxels can be wrapped into the same cluster. At this point, we can say that the first cluster is finalized. The algorithm will then pick up a voxel that currently has the largest t-value and is not clustered yet. This voxel is used as the initial center of a new cluster, and this cluster (the 2nd one) is formed by following the same "looking for the neighbors" and "looking for neighbors of

38

neighbors" procedures. Similarly, the 3rd and the following clusters are formed until all the voxels in the image are clustered. When the algorithm terminates, voxels marked with the same cluster number are in the same cluster. The detail of the algorithm is described as follows.

Data Structure

1. An array voxelList[N] is used to store all the voxels, where N is the number of voxels. A voxel has 6 fields, which structure is described below in an object-oriented manner.

```
class Voxel {
        int x, y, z; // the coordinates of this voxel
        double tvalue; // t-value of this voxel
        boolean isclustered; // the flag indicating whether the voxel is clustered
        int clusternumber; // which cluster this voxel is in
        public Voxel(int x1, y1, z1, double tvalue1) {
                x = x1;
                y = y1;
                z = z1;
                tvalue = tvalue1;
                isclustered = false; // initially the voxel is not clustered
                clusternumber = -1; // the voxel is initially in no cluster
          }
        }
```

2. An array adjVoxel[M] is used to store all the voxels that have valid coordinates and are adjacent to the current center voxel of the cluster that is being formed. M is the maximum number of adjacent voxels.

3. A stack voxelStack is used to store the neighboring voxels of the center voxel.

Algorithm

1.

// function segment(f, t) is for growing the ROIs

// Parameter "f" is the file containing x, y, z coordinates and t-value of each

// voxel in a descending order of t-values.

// Parameter "t" is the pre-determined threshold of t-value.

Segment (f, t):

BEGIN

    Let threshold = t and currentcluster = 0

    Initialize voxelList[N] with voxels using the information in file f

    Initialize "center" as the center voxel of a cluster, let center.x = center.y = center.z = -1 and center.tvalue = -1

    While there are un-clustered voxels in voxelList[N]

        Let currentcluster = currentcluster + 1

        Take an un-clustered voxel "top" that has the largest t-value as the initial center of the new cluster, let center.x = top.x, center.y = top.y, center.z = top.z, center.tvalue = top.tvalue

Let center.isclustered = true // mark the center voxel as clustered

Let center.clusternumber = currentcluster

FindNeighbor(center, threshold)

While voxelStack is not empty

Pop one voxel "oneneighbor" from voxelStack

// set "oneneighbor" as the new center voxel

Let center.x = oneneighbor.x, center.y = oneneighbor.y, center.z = oneneighbor.z, center.tvalue = oneneighbor.tvalue

FindNeighbor(center, threshold)

Endwhile

Endwhile

END

Algorithm

2.

// function findneighbor(center, threshold) is for finding the neighbors of the

// center voxel and push the neighboring voxels into voxelStack

// Parameter "center" is the current center voxel

// Parameter "threshold" is the pre-determined threshold of t-value

FindNeighbor(center, threshold):

BEGIN

Compute coordinates of all the voxels that are spatially connected to the center

voxel

For each voxel that is adjacent to the center voxel

    If the coordinates of the voxel are valid

        Insert the voxel into adjVoxel[M]

    Endif

Endfor

For each voxel "tempneighbor" in adjVoxel[M]

    If tvalue of center voxel and "tempneighbor" are both greater than or equal to or

both are less than the threshold

        // the voxel "tempneighbor" is a real neighbor

        Let tempneighbor.isclustered = true

        Let tempneighbor.clusternumber = center.clusternumber

        Push the voxel "tempneighbor" into voxelStack

    Endif

Endfor

Clear the array adjVoxel[M]

END

        After the region segmentation ended, we applied a feature ranking method [36] to select a small set of regions that were most relevant for classification of MCI. These most relevant regions were selected from the large quantities of regions determined by the region segmentation procedure. The rank score was the t-value of the initial center voxel (described in the flowchart in Figure 5.1) in each region. The GM intensities of these

initial center voxels were used as the features to train a classifier. According to our region segmentation method, we know that the initial center voxel of a region had the largest t-value with the neighboring voxels in the same region having similar t-values and was thus most discriminative in this region. Also, the regions with more discriminative power were identified earlier. We parametrically varied the number of ROIs used for classification to identify the number of ROIs that provided stable classification estimates and were unlikely to introduce overlearning. Specifically speaking, we tried different number of regions that were first segmented, starting from 5, 10, 15, and go on, and then identified the number of regions N that resulted in relatively higher classification accuracy. Although a large number of regions were identified by the region segmentation procedure, we did not try too many numbers of regions for two reasons. (1) As for a classifier, too many features may raise the problem of over-fitting and lead to worse classification performance. (2) We limited the number of regions to be selected to speed up the feature selection process. We then fine-tuned the number of regions around N to locate the regions which features could provide the highest classification accuracy.

LIBSVM [13, 51] was used to train a classifier with the selected features and evaluate the accuracy with leave-one-out cross validation. We used nonlinear SVM classification that constructed a hyper-plane to maximize the distance between MCI group and control group. The radial basis function (RBF) kernel ($C = 2.0, \gamma = 0.125$) was used in the work. We determined the best parameters (C, γ) by trying different pairs of values, and we picked the pair with the highest cross-validation accuracy.

5.4. Results

5.4.1. Pattern of MCI-specific Abnormalities

In our work, 19 ROIs were identified for classification of MCI subjects. The comparison between MCI and control group across the 19 ROIs demonstrated widespread effects of MCI, with the medial temporal lobe particularly affected, which is in accordance with the current findings in research of MCI. The effects of MCI can be seen in the gray matter probabilities of individual subjects. Figure 5.2 demonstrates that the influence of MCI on medial temporal lobe morphology can be observed in color scale for an MCI case compared to a control case. Color-coded visualization of ROIs can reflect the pathological severity of disease and can aid clinicians to identify the patterns of brain tissue atrophy in MCI subjects.
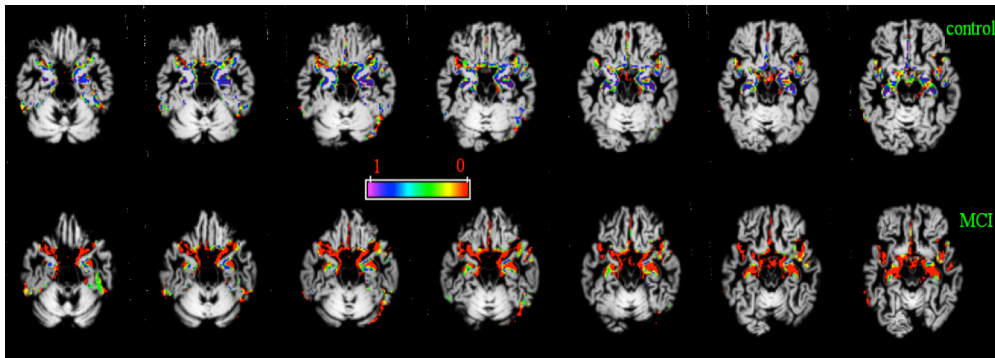
Figure 5.2 GM intensity map (slice 24 to slice 30) of the selected 19 ROIs in scans of one control (the upper row) and one MCI subject (the lower row). The control is female, right writing hand, age = 77, years of education = 1, SES = 4, MMSE = 29, CDR = 0. The MCI subject is female, right writing hand, age = 73, years of education = 4, SES = 3, MMSE = 27, CDR = 0.5. The color-coding shows the value of GM intensity for the individual subject using the color scheme represented by the color bar. The regions that are mostly blue in the upper row but are mostly red in the lower row are the atrophic regions in scans of MCI subjects.

5.4.2. Classification Accuracy

In our work, SVM classification using leave-one-out cross-validation provided a maximal 90% classification rate when using the MMSE and ROI data together in the SVM model. The sensitivity of this method was 92% and the specificity was 88%. This maximal classification accuracy was substantially higher than when using the MMSE score alone (79% accuracy). Figure 5.3 demonstrates that the MMSE and ROI variables together achieved the maximal classification accuracy when relatively few ROIs were included in the model (90% correct classification for 19 ROIs). Classification accuracy decreased with additional ROIs. In contrast, Figure 5.3 also shows that classification accuracy using the ROIs alone was relatively poor with few ROIs (81% correct classification for 19 ROIs) but increased to a high of 89% with an increasing number of ROIs.

The unexpected interaction between MMSE and the number of ROIs appeared to be driven by low gray matter volume in control cases and high total gray matter volume in MCI cases. Control cases who were misclassified with increasing ROIs were more likely to have lower total gray matter volumes than correctly classified control cases [mean of total gray matter volume for correctly classified control = 600.12 (7.71), mean of total gray matter volume for misclassified control = 474.11 (12.93), t = 51.06, df = 78, N = 80, two-tailed P < 0.0001]. MCI cases who were misclassified with increasing ROIs were more likely to have higher total gray matter volumes than correctly classified MCI cases [mean of total gray matter volume for correctly classified MCI = 518.37 (3.24),

mean of total gray matter volume for misclassified MCI = 591.69 (16.28), t = 14.83, df =

87, N = 89, two-tailed P < 0.0001]. The details are shown in Table 5.2.
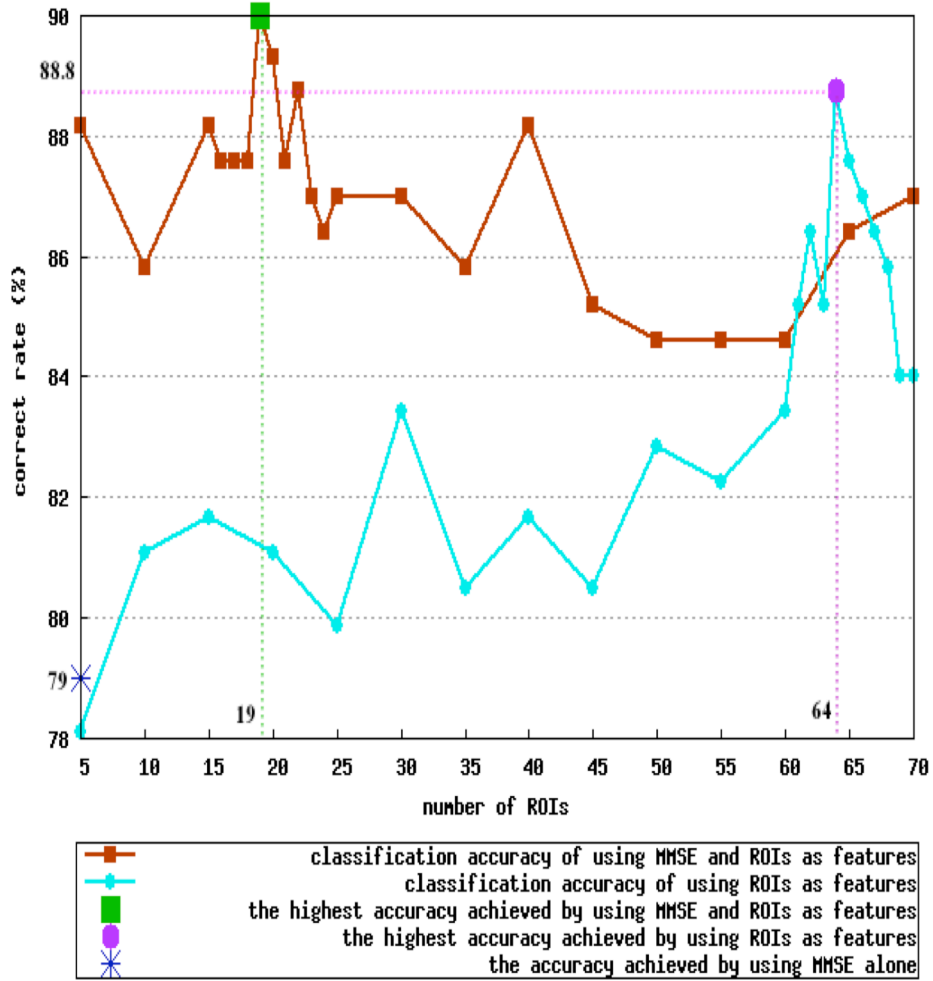
Figure 5.3 The plot of classification accuracy and the number of ROIs. If ROIs are the only features for classification, the number of features = the number of selected ROIs. If MMSE is included in the classification, the number of features = the number of selected ROIs + 1. Note that classification accuracy peaks for 19 ROIs when MMSE is included in the analysis and is subsequently variable with increasing number of ROIs. In contrast, classification accuracy increases with increasing number of ROIs when MMSE is not included and peaks for 64 ROIs. However, classification accuracy declines when additional ROIs are included and MMSE is not included.

Table 5.2 Total gray matter volume (mL) in MCI cases and control cases with increasing number of ROIs

# of ROIs	Gray matter volume for misclassified MCI	Gray matter volume for correctly classified MCI	Gray matter volume for misclassified control	Gray matter volume for correctly classified control
5	587.30	517.86	450.72	583.27
10	586.81	514.70	443.90	589.92
15	572.06	520.74	474.15	592.36
20	601.00	517.32	471.09	596.82
25	559.77	522.66	471.09	596.82
30	610.35	516.00	470.04	599.10
35	607.65	515.20	482.30	599.51
40	596.19	515.94	483.13	601.18
45	596.19	515.94	476.97	607.59
50	615.01	516.61	476.97	607.59
55	602.94	515.93	480.34	608.52
60	567.30	523.75	478.50	607.01
65	591.44	523.05	489.85	606.74
70	589.63	521.54	488.50	605.23

5.5.   Discussion

MCI classification has been performed with specific brain regions (e.g.
hippocampus) [28, 83] or several regions (patterns of the spatial distribution of brain
tissue atrophy) [19, 31, 30, 49, 63]. An important and unique finding from this study is
that MMSE and MRI-ROI data are relatively weak and unstable predictors of MCI when
studied separately, but together can provide robust and stable estimates for the probability
of having MCI. Interestingly, coupling data EEG and MRI measures has been shown to
improve classification rates for the early diagnosis of AD [68]. This suggests that MCI
classification with clinically sufficient sensitivity and specificity could be obtained with
the integration of measures from across different domains.

We observed relatively high classification accuracy using 15 – 30 ROIs, when
coupled with the MMSE score. Interestingly, classification accuracy decreased with
increasing number of ROIs when the MMSE score was included in the analysis. This
result appeared to occur because of an interaction between MMSE score and brain size.
Control cases with low total gray matter volume in control and MCI cases with high total
gray matter volume in MCI were more likely to be misclassified when many ROIs and
the MMSE score were included in the SVM. This result suggests that total gray matter
volume had an increasingly strong influence on classification with increasing numbers of
ROIs. One interpretation of these results is that classifiers for MCI should be developed
for specific gender and age cohorts.

Classification accuracy was high when 64 ROIs were included in the model
without the MMSE score. This approach is sub-optimal, however, because of the

likelihood of over-fitting and poor generalization when many variables are included in an SVM model. For example, classification accuracy declined when additional ROIs were included (>65 ROIs). Indeed, it is well known in machine learning field that the dimension of multivariate space needs to be decreased if the number of samples is not sufficient. As we examined only 169 subjects, a relatively small number of features would improve the reliability of the estimate of performance, provided they can accurately capture the structural abnormalities in MCI subjects.

One limitation of our results is that it is unclear which MCI cases will go on to develop AD, which cases may have some other forms of dementia, or which cases will exhibit cognitive decline that is expected for their age. Longitudinal studies [63] of MCI that incorporate large sample sizes will allow for cohort specific development of MCI classifiers, may have the most reliability, and provide greater confidence for guiding clinical planning than the classifier developed in this work. An additional limitation of classifiers for MRI data, in general, is that they are likely specific to the scanner from which the scans were acquired given that image intensities can vary according to sequence, scanner type, and head coil. For all of these reasons, the greatest clinical utility for these types of classification methods will be at large medical institutions where classifiers can be developed on the population base from that institution.

In the future, our method for detection of MCI will be evaluated with larger data sets. Meanwhile, longitudinal studies about whether MCI cases will continue to develop AD or which cases may have some other forms of dementia or some other possibilities will be carried out.

5.6.   Function of Image Classification in the CAD System

The classifier trained by our approach for detection of MCI is integrated in our

CAD system for classification of MCI. In this system, the function of image classification

is invoked after the image processing is finished. The trained model and the file of the 19

ROIs (with coordinates of initial center voxels of each ROI) are stored on the server to

assist the MCI diagnosis. A script will be used to select gray matter intensity values from

the initial center voxels of each of 19 ROIs in the uploaded image scans. The GM

intensity of the voxels combined with MMSE score form a test file. The test file is then

fed into the SVM classifier to predict the subject as MCI or normal by using the existing

trained model. Finally, an email that contains the link to the probability of MCI

classification is sent to the user. The link will direct the user to detailed information about

the classification probability and visual summary of the affected regions.

Figure 5.4 shows the implementation details of functions for image processing

and MCI detection in our system. An example of the post-processing information that is

provided for each subject is shown in Figure 5.5.

process.php

Start

Create a log file

collect the file information
and clinical information of
the subject

matlab.sh

run matlab.sh

Start

run hssc_cad.m

End

write the log file

predict.php

save the information
of the processing
results into database

Start

invoke
prediction.php

write the log file

End

form the file with GM
intensity values of
voxels in the 19 ROIs as
well as the MMSE value

feed the file into
the trained
classifier

send an email
containing prediction
results to the user

End

Figure 5.4 Implementation of the image processing and MCI detection in the CAD system

51
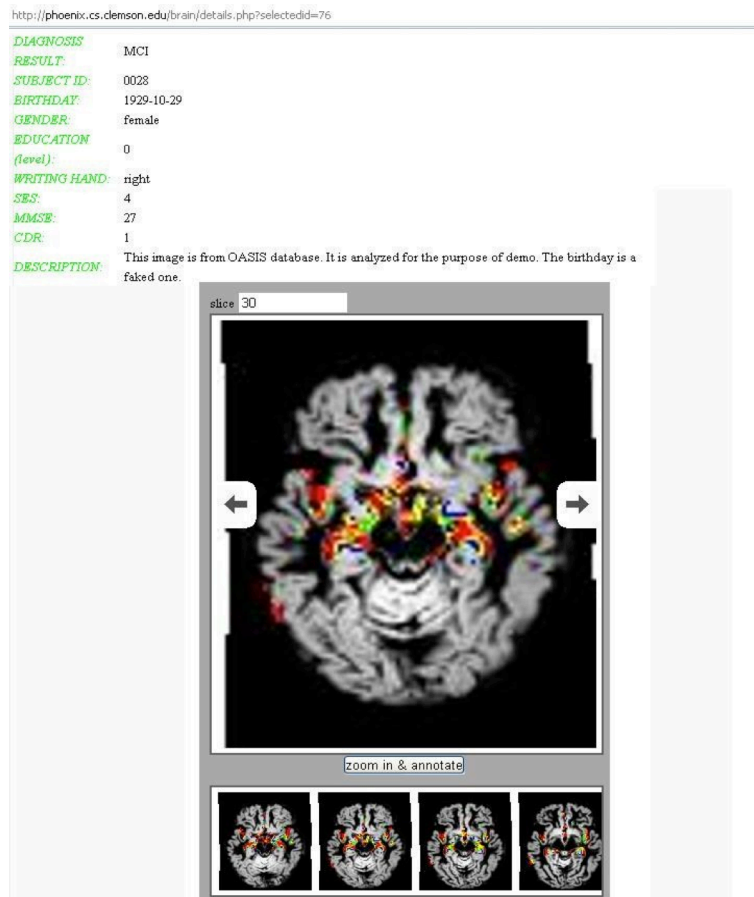
Figure 5.5 An example of the post-processing information that is provided for each subject. The box in the center is an image slice gallery (the current slice number is displayed on the top left corner), which presents the 2D slices of the image. Users can browse the slices back and forth by clicking the left and right arrows or view a particular slice by clicking on the corresponding icon (small size slice) listed in the bottom row. There are 91slices for one image, but only 4 slice icons are presented in the row. The 4 icons are changed to the ones with smaller slice numbers when users move the mouse over the leftmost icon or changed to the ones with larger slice numbers when users move the mouse over the rightmost slice icon in the row.

Chapter 6

Data Sharing and Other Functions

In addition to the functions for image processing and image classification, the CAD system also provides the capability for data sharing, knowledge sharing, visualization, and information storage and retrieval.

6.1.   Data Sharing

Although our preliminary study of MCI detection has achieved promising results, and the image data set used in our research is larger than the other studies in the same field, the data set is still limited because of subject privacy issue. A larger experimental data set with more people, more races, and more regions would help to achieve a more reliable and robust model so as to make a better prediction. To collect more experimental

data for MCI study, we encourage data sharing among different research sites through our CAD system. The image scans which are uploaded to our CAD system for detection of MCI will be added to the current dataset for training a more robust model. Moreover, researchers under IRB protocol may share the image scans in their respective research so as to collaboratively contribute to the diagnosis of MCI. De-identification is the first step for data sharing, which is a mandatory process to protect subject privacy. Two issues must be addressed for the purpose of image de-identification, which are anonymization and image defacing. The objective of anonymization is to de-identify the private subject information in the subject's image and demographic data file. On the other hand, image defacing aims to crop out or alter or mask the facial features. To protect privacy of subjects whose image scans are uploaded to our CAD system for detection of MCI and data sharing, we design a method for DICOM brain images de-identification. This method was presented in our work [54], and is now integrated into the CAD system. Users of our CAD system can use this function to de-identify the image scans on their own computers before uploading these scans into our system. This method can be extended to de-identify genetic or other forms of brain images (NIFTI, ANALYZE, EEG, etc.).

In the CAD system, the image de-identification function provides both the anonymization and the image defacing capabilities. Users can select the data items in the image header file and the demographic data file for anonymization and process them for a single or multiple subjects in a batch mode automatically, without the necessity of writing a script. Moreover, the anonymized data items are relabeled with random strings that are

54

the same as the strings for de-identifying DICOM image names. The image defacing

function does not need the construction of a brain mask or models of non-brain structures,

which therefore is easier to use. Visual inspection showed that the facial features were

removed successfully and the brain tissues were intact in our work.

6.1.1. Image Defacing

The image defacing function is for removing facial features. The function was

implemented based on the algorithm that we proposed for image defacing. Figure 6.1

presents the flowchart of the algorithm. Although the algorithm processes 2D image

slices, the defaced result can be rendered to 3D images with no facial features included.

Please note that the example of DICOM brain images in this work is provided by the

developer of DicomBrowser [26], courtesy of Denise Head. The three major steps of the

image defacing algorithm are briefly described below.
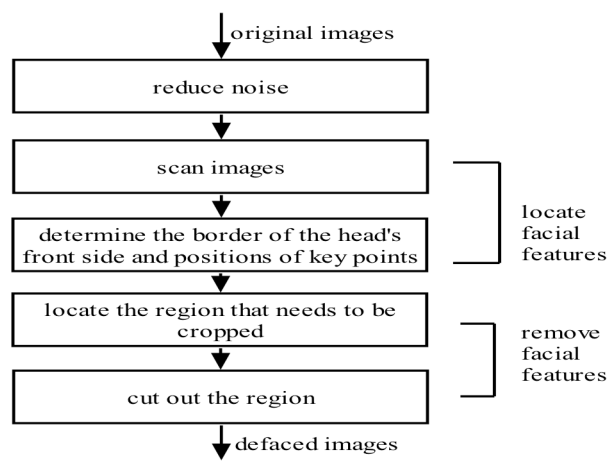
Figure 6.1 The flowchart of the image defacing algorithm

1) Noise reduction.

We observed that too much noise existed in the DICOM images, thus we applied EdgeFilter and MinimumFilter [45] to remove the noise on the images. Figure 6.2 shows an example of the original image slice. The noise reduction effect on this slice is shown in Figure 6.3.

Figure 6.2 A 2D image slice (sagittal) that explicitly shows the facial features
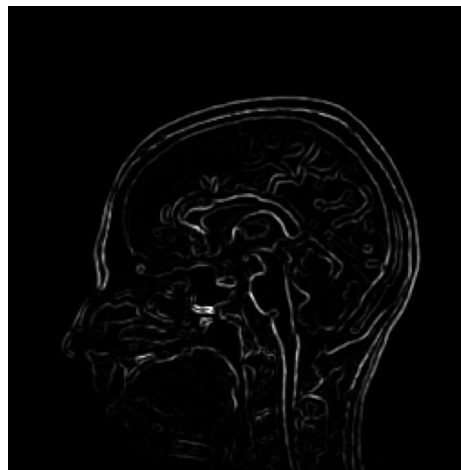
Figure 6.3 A 2D image slice (sagittal) after noise reduction

2) Facial features locating.

Firstly, after noise reduction, the image slices (sagittal) were scanned from top to bottom vertically, and from left to right on each horizontal plane. The scanning result is presented in Figure 6.4. The border of the head's front side was then determined according to the RGB values of the points in the images.
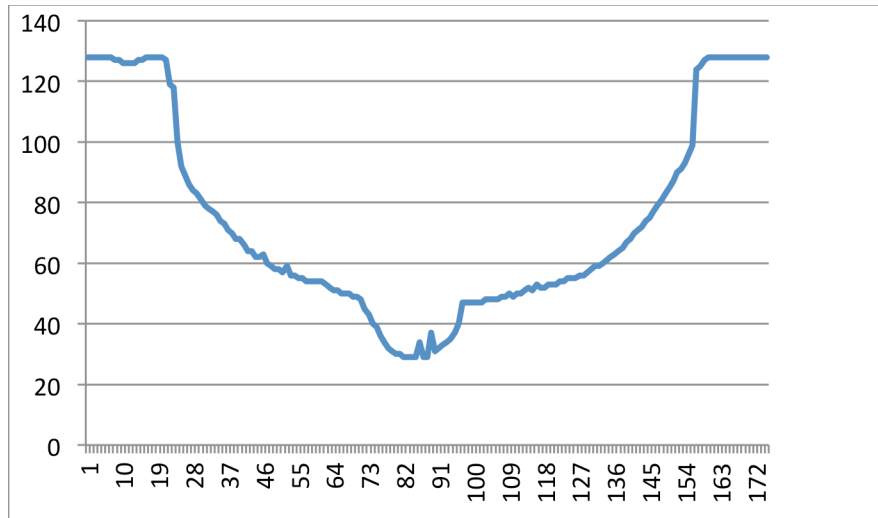
Figure 6.4 The scanning result of the experimental image slices. The x-axis refers to the image slice number. And the y-axis is the x coordinates of the most left points in each slice.

Secondly, the positions of some key points on a subject's face could be determined based on the scanning result. As is known, the most protruding point of a subject's nose has the smallest x coordinate, which hence could be identified by the lowest point on the curve in Figure 6.4. Then we took the slice which the lowest point on the curve was in, scanned it from top to bottom and from left to right, and then watched the variance of x coordinates of the most left points on continuous y coordinates. With respect to the points located in the image slices from the head's top to the nose, the x coordinates usually gradually decrease until a minimum value (i.e. the x coordinate of the most protruding

57

point on the forehead, say point A), and then slowly increase to a maximum value (i.e. the top point on the bridge of the nose), and finally decrease until another minimum value (i.e. the x coordinate of the most protruding point of the nose, say point B). Therefore, by watching the variance of x coordinates, point A and point B could be identified. We then looked for the point C with x coordinate equaled 0 and y coordinate equaled y_B. From point A, we drew a vertical line downwards; and from point C, we drew a horizontal line. The intersection point of the two lines was point D. Next, we found the mirror point E of point B using point D as the center. Besides, we found the point F at $(x_E, \frac{y_A + y_B}{2})$. The positions of these points were determined according to the usual distance between facial features and the structure of brain. All these points are marked in Figure 6.5.

Figure 6.5 A 2D image slice (sagittal) in which facial features have been cut out. Its original image (before defacing) is presented in Figure 6.2.

3) Facial features removing.

The points found in the previous step outlined the region that needed to be cut out. Specifically, we linked point A and point F, point A and point C. We then drew a vertical line e from point F through E downwards, and drew a vertical line e' from point B downwards. B' is the point with y coordinate equaled 0 on line e', and E' is the point with y coordinate equaled 0 on line e. Finally, the area ACB'E'FA (see Figure 6.5) was cut out. Obviously, the image was defaced by removing this area.

6.1.2. Image Anonymization

The anonymization function allows users to select data items in the image header files and the demographic data files, and then automatically replaces the data with randomly created strings. The flowchart is shown in Figure 6.6.

the selected data items
the DICOM image files
the demographic and behavioral data file

create a random string

replace the data items with the string

mark the DICOM files with the string

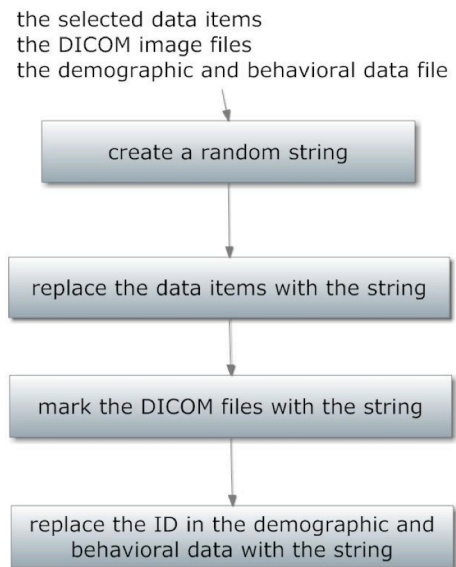replace the ID in the demographic and
behavioral data with the string

Figure 6.6 The flowchart of anonymization

6.1.3. Results

The experimental results showed that the DICOM images could be anonymized by our method without losing connection between images and demographic/behavioral data of the same subject. In addition, it turned out that the images could be properly defaced, with no brain tissue removed. Also, our algorithm makes sure that the cutting point can adjust automatically according to the size of the brain. The 2D image slices can be rendered to a 3D image, as shown in Figure 6.7.
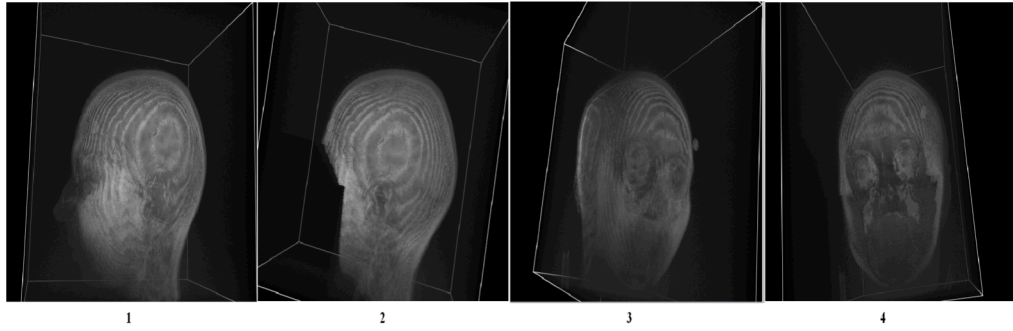
Figure 6.7 Image 1 (sagittal) is the rendered 3D image before defacing. Image 2 (sagittal) is the rendered image after defacing. Image 3 and 4 demonstrate the image before and after defacing from other angles.

Our method has been tested with more image data sets, however, the images and their results cannot be presented here due to IRB restriction. Since different researchers may prefer different methods for de-identifying brain images, in the future, we will further extend the brain image de-identification function to include other algorithms. There are two other options for defacing algorithm. One is replacing the approach of cropping out facial features with the approach of masking the facial features. Cropping out facial features may mistakenly cut out a portion of brain tissue. Instead, the approach

of masking does not have such a risk because it adds a mask over facial features. The other option is to cut the image with a straight line (e.g. link point A and point E' in Figure 6.5) rather than curved lines. This may be simpler than the current approach, and may reduce the risk of cutting out the brain tissue. In addition, the de-identification function will be expanded to process genetic or other forms of images (e.g. ANALYZE, NIfTI, EEG, etc.).

6.1.4. Integration

The image de-identification function, including the anonymization of data items in the image header files and the demographic/behavioral data files, as well as the defacing of facial features of a subject's image, has been integrated in our CAD system for the purpose of data sharing. The function is wrapped as a tool that is embedded in the CAD system from which users can download the tool to their own sites for de-identifying images. The image de-identification cannot happen in the CAD system because of the safety consideration. Researchers and clinicians would like the images of their sites be de-identified on their local machines before they submit the images to our CAD system for data sharing and disease diagnosis. The function is developed with Java, and it runs on Windows operating system with Java Runtime Environment (JRE) installed. Users can start the image de-identification on their own computers by running a Windows batch file.

Figure 6.8 and Figure 6.9 present interfaces of anonymization in the image de-identification function, which are for the anonymization of data items in the image header files and the demographic/behavioral data files. Figure 6.8 shows the information in the

image header files. To anonymize an image, users can select the data items in the image

header files that need to be hided and include the demographic/behavioral data, as shown

in Figure 6.9. The subject's ID in the DICOM image header files and the ID that labels

the subject's file names are replaced with the same random string. Besides, the ID in the

subject's demographic and behavioral data is also anonymized with the same string. In

this way, the images, data items of the header files, and the demographic and behavioral

information of this subject are connected together.
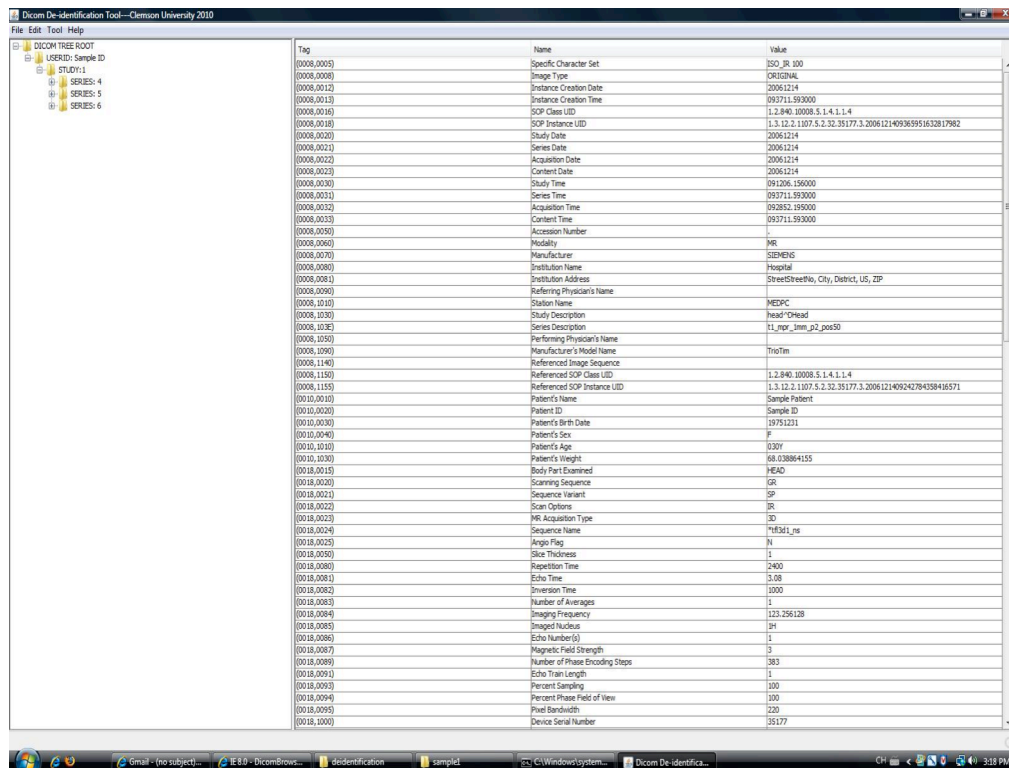
Figure 6.8 The interface of anonymization in the image de-identification function, for the anonymization of data items in the image header files. The left panel shows the cascaded structure of the image files. There are 3 series in the experimental data set. The right panel shows the data items in the image header of the current image. The first column is the tag of the data item, the second column is the item's name, and the last column is the item's value.

As for the image defacing in the image de-identification function, users can right click on a specific image slice to view an image before and after image defacing. The image slice is displayed with imageJ [44], as presented in Figure 6.10. In addition, users can deface one image or multiple images by choosing the directory of the images to be processed and the directory for storing the defaced images, as demonstrated in Figure 6.11.
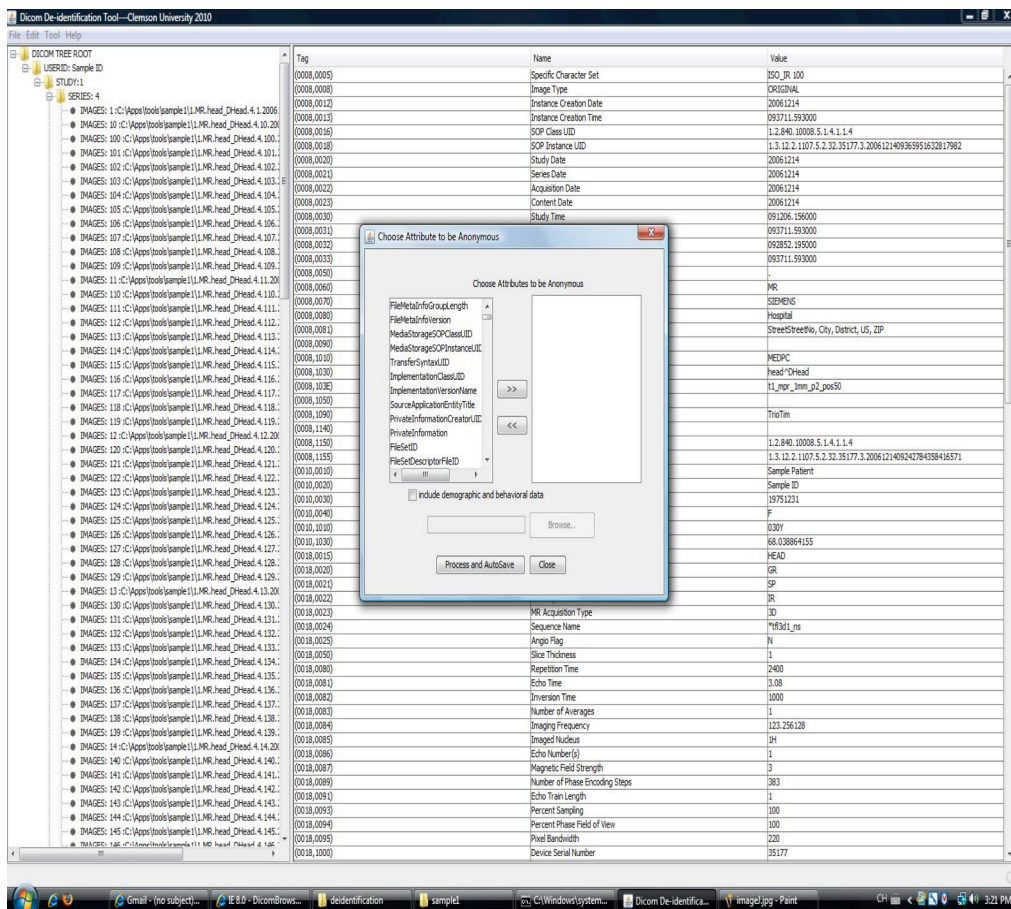

Figure 6.9 The interface for users to select data items in the image header files and to include demographic data files for anonymization
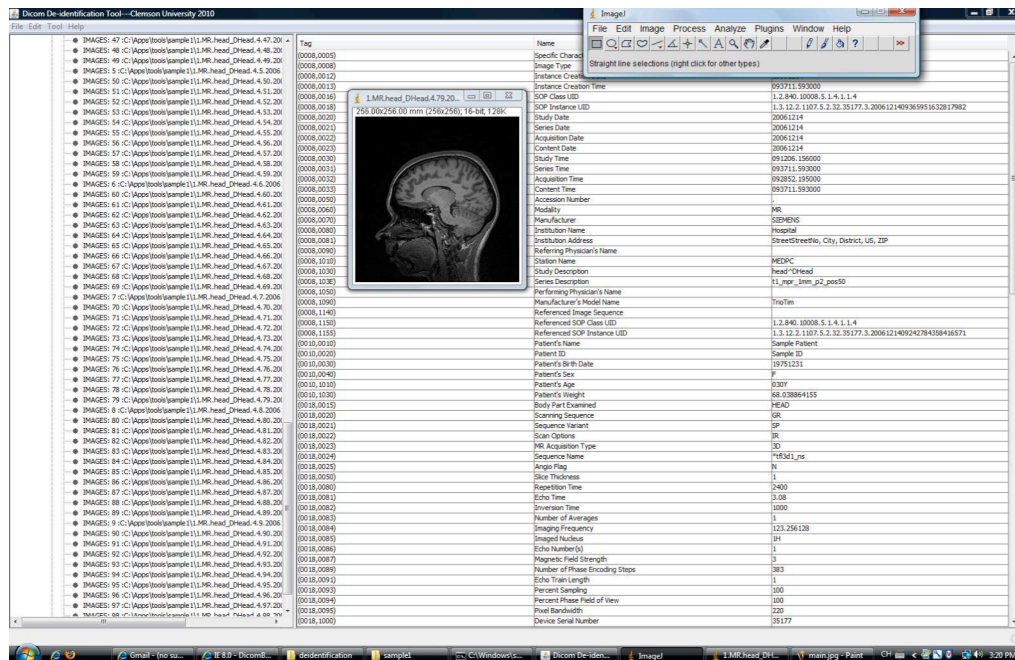
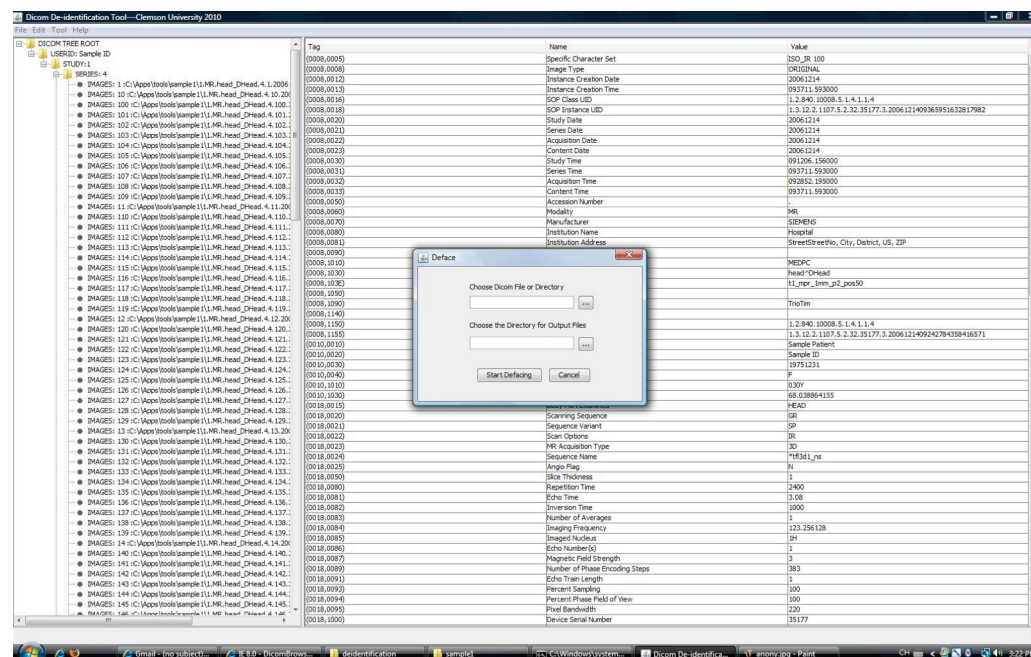Figure 6.10 The screenshot of viewing an image slice with imageJ

Figure 6.11 The interface for users to do image defacing

6.2.   Knowledge Sharing

In the CAD system, the image annotation function is for knowledge sharing among researchers to collaboratively contribute to diagnosis of disease. With this function, clinicians can mark the brain regions that are correlated to the disease and they can put comments on the regions to indicate its association with the disease. Other researchers can read these comments so as to understand the ROIs or they can add comments with their understanding of the regions. Users can insert, modify or remove an annotation within their privilege as needed. An annotated coordinate is marked with a special marker. When a user clicks on a maker, annotations will be displayed in a pop-up window. An example of the image annotation function is shown in Figure 6.13.

6.3.   Visualization

In the CAD system, the brain images will be displayed as 2D slices, and users can browse the image slices back and forth in the image gallery. The ROIs will be colored and the color coding shows the value of GM intensity using the rainbow color scheme. Users can adjust the threshold of GM intensity through a color bar or direct input values to get a different view of ROIs. Only regions with GM intensity exceeding the threshold will be displayed with colors. Users can also zoom into a particular image slice to examine the details of this slice.
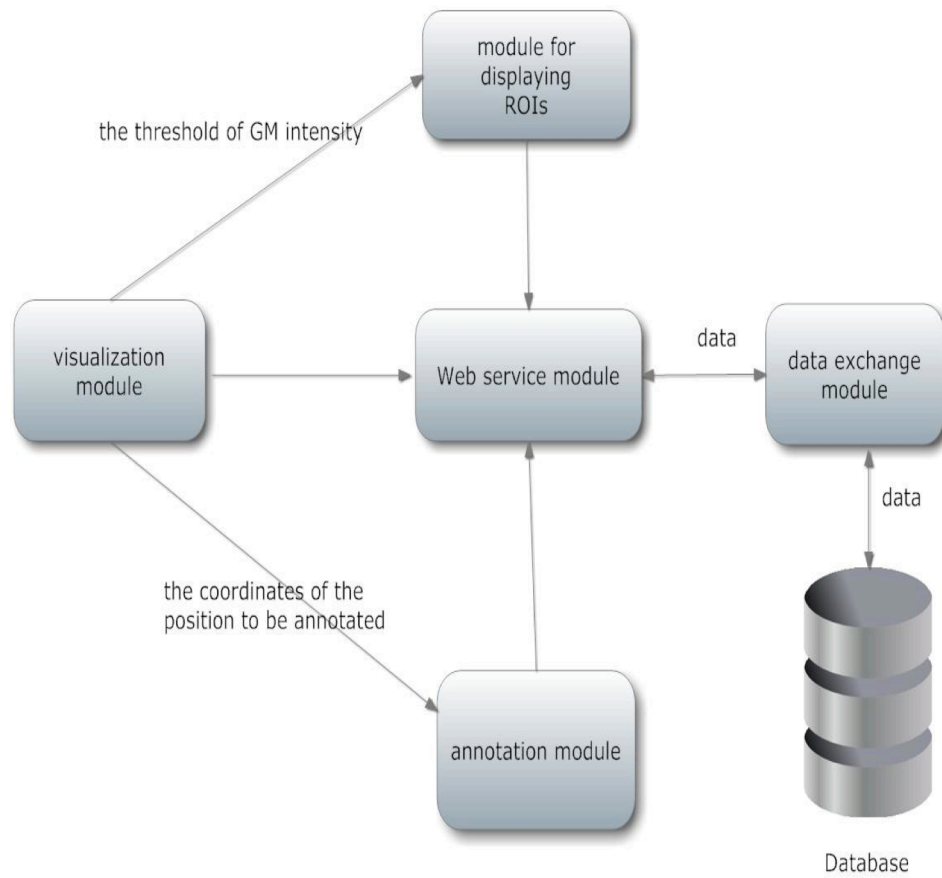
Figure 6.12 Interaction of modules in the image visualization and annotation functions

The image visualization function and the image annotation function are implemented by the following 5 modules. The interaction of the 5 modules is presented in Figure 6.12. And an example of the image visualization function is shown in Figure 6.13.

(1) Visualization module. This module implements the image visualization functions, including image slice navigation, zoom in/out functions and adjustment of the threshold of GM intensity.

(2) Module for displaying ROIs. This module changes the display of ROIs through a server-side PHP program based on the threshold set by users.

(3) Annotation module. This module implements image annotation functions. Users can add, delete and edit the annotation information at a certain coordinate of an image slice.

(4) Web service module. PHP programs run on the Web server to handle the service logic and interact with the data server.

(5) Data exchange module. This module handles the data exchange between the other modules and the database.
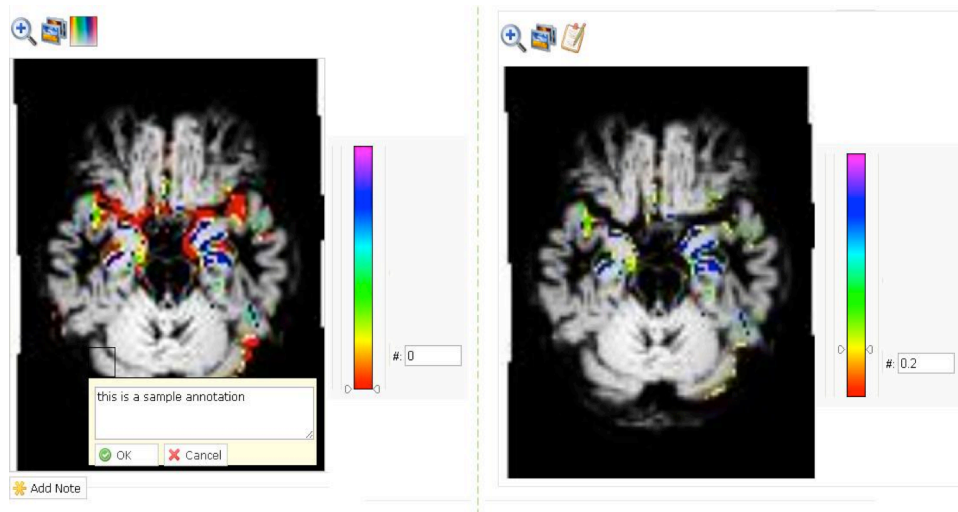
Figure 6.13 An example of the visualization and annotation function. The left image shows the annotation function. When users click the "Add Note" button on the lower left corner, the annotation panel (the white rectangle panel), which can float over the image slice, will pop up. Users can insert, modify or delete the annotation as needed. The cursor on the color bar indicates the GM intensity threshold that can be set from 0 to 1 by sliding the cursor along the color bar or setting a value in the textbox on the right side of the bar. Voxels with GM intensity beyond the threshold are colored using the color scheme of the color bar. If the cursor is on the lower end (red), the threshold is set to 0; if it is on the upper end (purple), the threshold is 1. The colorful regions overlaying on the left image slice are the voxels with GM intensity over the threshold 0. With the same slice, these regions shrink when the threshold is set to 0.2, as shown on the right part of figure.

6.4.   Information Storage and Retrieval

Users can upload de-identified MRI scans (Analyze format) and the related

clinical and demographic information, which will be stored in the database of the CAD

system. After the image is processed, the processing results are physically stored in the

file system with their paths stored in the database and associated with the patient's

clinical and demographic information. The image processing results include segmentation,

normalization, modulation and smoothing results, as well as a stack of 2D image slices

and files with intensity of voxels for each slice. Moreover, the diagnosis prediction

(probability of MCI or normal) is saved in the database. In the CAD system, the database

also stores the account information. Users can choose which accounts in the system to

share the files with when they upload an image file. An image file can only be accessed,

processed, visualized and annotated by its owner (the user who uploaded the image) and

the users with appropriate permission levels authorized by the owner. With this scheme,

users of the system can collaboratively analyze the brain images. Furthermore, users can

retrieve the images and demographic information of subjects by some search options (e.g.

age, gender, etc.). Figure 6.14 shows a search result that includes the diagnosis result and

the subject's clinical and demographic information and a link to the detailed information

as well.

Figure 6.14 An example of the search result in the CAD system

Chapter 7

Conclusions and Future Work

In this work, we propose a complete CAD system for early and automated detection of MCI. The CAD system can provide functions for image processing, classification of MCI subjects, image visualization, image annotation, image de-identification, and data storage and retrieval. Privacy issues notwithstanding, our system could be implemented for multiple institutions given the increase in Internet bandwidth and decrease in storage costs. Compared with the desktop applications, our system would be easier to use because it is Web-based. Users would not need to install any software to use the system. Importantly, our Web-design can enable a team of physicians and supporting staff to access patient results and work collaboratively through the annotation function with the goal of increasing communication and enhancing clinical planning. To

70

the best of our knowledge, this Web-based CAD system will be the first one to provide

the capability of CAD for MCI. The CAD system is designed to be expandable because

of its component architecture. Hence, this system can be extended to detect other forms

of subtle brain injury where early detection will enhance patient treatment, as long as

scripts of image preprocessing and trained classifiers are available. Two major

components need to be replaced for detection of other subtle diseases. One component is

for image processing, in which scripts can be customized for different types of images.

The other component is for disease detection, which requires the customization of scripts

and the training of classifiers specific to certain diseases.

The following publications have resulted from this research:

Lin Li, James Z. Wang, Carl Lozar, and Mark A. Eckert, "Automated Detection of Mild

Cognitive Impairment through MRI Data Analysis", International Journal on Artificial

Intelligence Tools, to appear.

Lin Li, James Z. Wang, "DDIT – A Tool for DICOM Brain Images De-identification",

the Proceeding of the 5th International Conference on Bioinformatics and Biomedical

Engineering, Wuhan, China, May 10 – 12nd, 2011, pp. 1 - 4.

Lin Li, Carl Lozar, Mark A. Eckert, Dheeraj Chahal, James Z. Wang, "Detection of Mild

Cognitive Impairment using Image Differences and Clinical Features", the Proceeding of

the 10th IEEE International Conference on Bioinformatics and Bioengineering, Thomas

Jefferson University, Philadelphia, PA, USA, May 31 - June 3rd, 2010, pp. 106 - 111.

Lin Li, Carl Lozar, Mark A. Eckert, Dheeraj Chahal, James Z. Wang, "Online Brain

Image Database System for Diagnosis of Subtle Brain Injury", the Proceeding of the 4th

International Conference on Bioinformatics and Biomedical Engineering, Chengdu, China, June 18 - 20th, 2010, pp. 1 - 4.

There are several directions for the future work. The first aim is to improve the classification of MCI, by developing scanner specific classifiers, and validation with a much larger data set diversified across different regions and races. Secondly, many existing MRI data analysis tools are standalone or command line applications that need to be installed by researchers or physicians on their local computers. Most tools for neuroimaging studies in Biomedical Informatics Research Network (BIRN) [47], such as the Extensible Neuroimaging Archive Toolkit (XNAT) [57], are designed for general neuroimaging studies, not specifically for MCI early detection. Therefore, there is an urgent need to adapt the existing tools and integrate them into a community-based platform exclusive for MCI study. So our second goal is to build a collaborative cloud computing infrastructure in which researchers and physicians can share their computing expertise, computational resources, image data, analysis tools, and biomedical knowledge in MCI studies.

Bibliography

[1] R. Adams, and L. Bischof, Seeded region growing, *IEEE Transactions on Pattern Analysis and Machine Intelligence*, 16(6):641 - 647, 1994.

[2] J. Ashburner, and K.J. Friston, Voxel based morphometry – the method. *NeuroImage,* 11(6): 805 – 821, 2000.

[3] J. Ashburner, and K.J. Friston, Unified segmentation. *Neuroimage,* 26:839 – 851, 2005.

[4] A. Bischoff-Grethe, B. Fischl, I.B. Ozyurt, et al., A technique for the deidentification of structural brain MR images, *Human Brain Mapping*, 28(9):892 - 903, 2007.

[5] C.M. Bottino, C.C. Castro, R.L. Gomes, et al., Volumetric MRI measurements can differentiate Alzheimer's disease, mild cognitive impairment, and normal aging. *Int Psychogeriatr*, 14:59 – 72, 2002.

[6] M. Bozzali, M. Filippi, G. Magnani, et al., The contribution of voxel-based morphometry in staging patients with mild cognitive impairment. *Neurology*, 67:453 – 460, 2006.

[7] H. Braak, and E. Braak, Evolution of the neuropathology of Alzheimer's disease, *Acta Neurol Scand Suppl,* 165:3 – 12, 1996.

[8] D. Bradley, and G. Roth, Adaptive thresholding using the integral image, Journal of Graphics, GPU, & Game Tools 12 (2) (2007) 13–21.

[9] "BrainStorm", [Online], Available: http://neuroimage.usc.edu/brainstorm/.

[10] J.B. Brewer, Fully-automated volumetric MRI with normative ranges: translation to clinical practice. *Behabioural Neurology,* 21:21 – 28, 2009.

[11] E.J. Burton, R. Barber, E.B. Mukaetova-Ladinska, et al., Medial temporal lobe atrophy on MRI differentiates Alzheimer's disease from dementia with Lewy bodies and vascular cognitive impairment: a prospective study with pathological verification of diagnosis. *Brain*, 132 (1):195 – 203, 2009.

[12]"CADstream",[Online],Available: http://www.merge.com/products/cadstream/index.aspx.

[13] C.C. Chang, and C.J. Lin, LIBSVM: a library for support vector machines. Software available at http://www.csie.ntu.edu.tw/~cjlin, 2001.

[14] G. Chételat, B. Desgranges, V. de la Sayette, et al., Mapping gray matter loss with voxel-based morphometry in mild cognitive impairment. *Neuroreport*, 13 (15):1939 – 1943, 2002.

[15] G. Chételat, B. Landeau, F. Eustache, et al., Using voxel-based morphometry to map the structural changes associated with rapid conversion in MCI: a longitudinal MRI study. *Neuroimage*, 27:934 – 946, 2005.

[16] O. Colliot, G. Che´ telat, M. Chupin, et al., Discrimination between Alzheimer disease, mild cognitive impairment, and normal aging by using automated segmentation of the hippocampus. *Radiology,* 248:194 – 201, 2008.

[17] "Computer-enhanced breast MR analysis streamlines workflow and generates more robust information", [Online], Available: http://www.icadmed.com/products/breast/pdf/SpectraLook%20Sellproof.pdf.

[18] B. Cramariuc, M. Gabbouj, and J. Astola, Clustering based region growing algorithm for color image segmentation, In *Proceedings of the 13th International Conference on Digital Signal Processing*, pp. 857 - 860, 1997.

[19] C. Davatzikos, Y. Fan, X. Wu, et al., Detection of prodromal Alzheimer's disease via pattern classification of MRI. *Neurobiol Aging*, 29:514 – 523, 2008.

[20] P. Delaere, C. Duyckaerts, J.P. Brion, et al., Tau, paired helical filaments and amyloid in the neocortex: a morphometric study of 15 cases with graded intellectual status in aging and senile dementia of Alzheimer type. *Acta Neuropathol,* 77:645 – 653, 1989.

[21] M.J. De Leon, S. DeSanti, R. Zinkowski, et al., Longitudinal CSF and MRI biomarkers improve the diagnosis of mild cognitive impairment. *Neurobiol Aging*, 27:394 – 401, 2006.

[22] "Dementia", [Online], Available: http://www.ncbi.nlm.nih.gov/pubmedhealth/PMH0001748/.

[23] R.S. Desikan, H.J. Cabral, C.P. Hess, et al., Automated MRI measures identify individuals with mild cognitive impairment and Alzheimer's disease. *Brain*, 132:2048 – 2057, 2009.

[24] "DICOM", [Online], Available: http://medical.nema.org/.

[25] "DICOM (Digital Imaging and Communications in Medicine)", [Online], Available: http://www.ms-technology.com/resource-center/dicom.html.

[26] "DicomBrowser", [Online], Available: http://nrg.wustl.edu/projects/DICOM/DicomBrowser.jsp.

[27] Z. Doychev, Basics of Medical Image Segmentation and Registration, [Online], Available: http://campar.in.tum.de/twiki/pub/Chair/TeachingWs05SegmentationRegistrationHauptseminar/02DoychevEdgesFeaturesHandout.pdf

[28] A.T. Du, N. Schuff, D. Amend, et al., Magnetic resonance imaging of the entorhinal cortex and hippocampus in mild cognitive impairment and Alzheimer's disease. *J Neurol Neurosurg Psychiatry*, 71:441 – 447, 2001.

[29] E.J. Escott, and D. Rubinstein, Free DICOM image viewing and processing software for your desktop computer: what's available and what it can do for you. *RadioGraphics*, 23:1341 - 1357, 2003.

[30] Y. Fan, N. Batmanghelich, C.M. Clark, et al., Spatial patterns of brain atrophy in MCI patients, identified via high-dimensional pattern classification, predict subsequent cognitive decline. *Neuroimage*, 39:1731 – 1743, 2008.

[31] Y. Fan, S.M. Resnick, X. Wu, et al., Structural and functional biomarkers of prodromal Alzheimer's disease: A high-dimensional pattern classification study. *Neuroimage*, 41 (2):277 – 285, 2008.

[32] Y. Fan, D. Shen, and C. Davatzikos, Classification of structural images via high-dimensional image warping, robust feature extraction, and SVM. In: *Lecture Notes in Computer Science*. Springer-Verlag GmbH, 2005.

[33] D.R. González, T. Carpenter, J. I. van Hemert, et al., An open source toolkit for medical imaging deidentification, *European Society of Radiology*, 20(8):1896 - 1904, 2010.

[34] R.C. Gonzalez, and R.E. Woods, Digital Image Processing, 2nd Edition, Prentice Hall.

[35] M. Grundman, R.C. Petersen, S.H. Ferris, et al., Mild cognitive impairment can be distinguished from Alzheimer disease and normal aging for clinical trials. *Arch. Neurol.*, 61(1): 59 – 66, 2004.

[36] I. Guyon, and A. Elisseeff, An introduction to variable and feature selection. *J Mach Learn Res,* 3:1157 – 1182, 2003.

[37] H.K. Hahn, and H. Peitgen, The skull stripping problem in MRI solved by a single 3D watershed transform, In *Proc. MICCAI, LNCS*, 1935:134 - 143, 2000.

[38] A. Hämäläinen, S. Tervo, M. Grau-Olivares, et al., Voxel-based morphometry to detect brain atrophy in progressive mild cognitive impairment. *Neuroimage*, 37:1122 – 1131, 2007.

[39] Y. Hirata, H. Matsuda, K. Nemoto, et al., Voxel-based morphometry to discriminate early Alzheimer's disease from controls. *Neurosci Lett*, 382:269 – 274, 2005.

[40] S.A. Hojjatoleslami, and J. Kittler, Region growing: a new approach, *IEEE Transactions on Image Processing*, 7(7):1079 - 1084, 1998.

[41] "iCAD: Products - Breast MRI CAD", [Online], Available: http://www.hyperactive.to/icad_07/products/breast/breastmri.htm.

[42] "iCAD: Products - Prostate MRI CAD", [Online], Available: http://www.hyperactive.to/icad_07/products/prostate/prostatemri.htm.

[43]"ICBMTemplate",[Online],Available: http://www.loni.ucla.edu/Atlases/Atlas_Detail.jsp?atlas_id=5.

[44] "ImageJ", [Online], Available: http://rsbweb.nih.gov/ij/.

[45] "JH LABS", [Online], Available: http://www.jhlabs.com/ip/filters/index.html.

[46] G.B. Karas, P. Scheltens, S.A.R.B. Rombouts, et al., Global and local gray matter loss in mild cognitive impairment and Alzheimer's disease. *Neuroimage*, 23:708 – 716, 2004.

[47] D.B. Keator, J.S. Grethe, D. Marcus, et al., A national human neuroimaging collaboratory enabled by the biomedical informatics research network (BIRN). *IEEE Transactions on Information Technology in Biomedicine, Special Bio-Grid edition*, 12(2):162 - 172, 2008.

[48] R.J. Killiany, M.B. Moss, M.S. Albert, et al., Temporal lobe regions on magnetic resonance imaging identify patients with early Alzheimer's disease. *Arch Neurol*, 50:949 – 954, 1993.

[49] S. Klöppel, C.M. Stonnington, C. Chu, et al., Automatic classification of MR scans in Alzheimer's disease. *Brain*, 131:681 – 689, 2008.

[50] M.J. Kuhn, M. Wendel, T. Gleason, et al., The use of Z3d software in breast MRI to improve sensitivity and specificity in the diagnosis of malignant neoplasms. *SPIE*. http://www.clariomedical.com/pdf/publications/SPIE_Abstract.pdf, 2009.

[51] "LIBSVM",[Online],Available: http://www.csie.ntu.edu.tw/~cjlin/libsvm/index.html.

[52] L. Li, C. Lozar, M.A. Eckert, et al., Detecion of mild cognitive impairment using image differences and clinical features. In *Proc. the 10th IEEE International Conference on Bioinformatics and Bioengineering*, pp.106 – 111, 2010.

[53] L. Li, C. Lozar, M.A. Eckert, et al., Brain image database system for diagnosis of subtle brain injury. In *Proc. of the 4th International Conference on Bioinformatics and Biomedical Engineering*, pp: 1 -4, 2010.

[54] L. Li, and J.Z. Wang, DDIT – a tool for DICOM brain images de-identification. In *Proc. of the 5th International Conference on Bioinformatics and Biomedical Engineering*, pp: 1 – 4, 2011.

[55] M. Mancas, B. Gosselin, and B. Macq, Segmentation using a region growing thresholding, In *Proceedings of the SPIE,* 5672:388 – 398, 2005.

[56] D.S. Marcus, A.F. Fotenos, J.G. Csernansky, et al., Open Access Series of Imaging Studies: longitudinal MRI data in nondemented and demented older adults. *J Cogn Neurosci* 22(12):2677 – 2684, 2009.

[57] D.S. Marcus, T. Olsen, M. Ramaratnam, et al., The extensible neuroimaging archive toolkit (XNAT): an informatics platform for managing, exploring, and sharing neuroimaging data. *Neuroinformatics,* 5(1):11 - 34, 2007.

[58] D.S. Marcus, T.H. Wang, J. Parker, et al., Open Access Series of Imaging Studies (OASIS): Cross-sectional MRI Data in young, middle aged, nondemented, and demented older adults. *Journal of Cognitive Neuroscience*, 19:1498 - 1507, 2007.

[59] "Mbirn: Defacer for structural MRI - NAMIC", [Online], Available: http://www.namic.org/Wiki/index.php/Mbirn:_Defacer_for_structural_MRI.

[60] F. Meyer, and S. Beucher, Morphological segmentation, *J. Vis. Commun. Image Represent.*, 1:21- 46, 1990.

[61] S. Mikula, J.M. Stone, and E.G. Jones, BrainMaps.org – interactive high-resolution digital brain atlases and virtual microscopy, *Brains, Minds & Media*, vol. 3, 2008.

[62] "Mild Cognitive Impairment (MCI) What do we do now?", [Online], Available: http://www.gerontology.vt.edu/docs/Gerontology_MCI_final.pdf.

[63] C. Misra, Y. Fan, and C. Davatzikos, Baseline and longitudinal patterns of brain atrophy in MCI patients, and their use in prediction of short-term conversion to AD: results from ADNI. *Neuroimage*, 44:1415 – 1422, 2009.

[64] J.C. Morris, The Clinical Dementia Rating (CDR): current version and scoring rules. *Neurology,* 43:2412 – 2414, 1993.

[65] J.P. Mugler, and J.R. Brookeman, Three-dimensional magnetization-prepared rapid gradient-echo imaging (3D MP RAGE). *Magn Reson Med,* 15:152 – 157, 1990.

[66] "OASIS", [Online], Available: http://www.oasis-brains.org/.

[67] H. Papasaika, Segmentation: Introduction to Signal- and Image-Processing. [Online], Available: http://www.igp.ethz.ch/photogrammetry/education/lehrveranstaltungen/RSGISFS2011/coursematerial/segmentation.pdf.

[68] T. Patel, R. Polikar, C. Davatzikos, et al., EEG and MRI data fusion for early diagnosis of Alzheimer's disease. In *Proc. of 30th Annual International IEEE EMBS Conference*, pp. 1757 – 1760, 2008.

[69] C. Pennanen, C. Testa, M.P. Laakso, et al., A voxel-based morphometry study on mild cognitive impairment. *J Neurol Neurosurg Psychiatry*, 76:11 – 14, 2005.

[70] R.C. Petersen, Mild Cognitive Impairment: Aging to Alzheimer's Disease. Oxford University Press, 2003.

[71] R.C. Petersen, R. Doody, A. Kurz, et al., Current concepts in mild cognitive impairment. *Arch Neurol,* 58: 1985-1992, 2001.

[72] O.S. Pianykh, Digital Imaging and Communications in Medicine (DICOM): A Practical Introduction and Survival Guide. Springer, 2008, Chapter 11.

[73] Progress Report on Alzheimer's Disease 2004-2005. In: *Services USDoHaH*, ed., 2005.

[74] F. Se´gonne, A.M. Dale, E. Busa, et al., A hybrid approach to the skull stripping problem in MRI, *NeuroImage*, 22:1060 - 1075, 2004.

[75] M. Sezgin, and B. Sankur, Survey over image thresholding techniques and quantitative performance evaluation. *Journal of Electronic Imaging,* 13(1):146 – 168, 2004.

[76] F.Y. Shih, and S. Cheng, Automatic seeded region growing for color image segmentation, *Image and Vision Computing*, 23:877 - 886, 2005.

[77] M.R. Siadat, H. Soltanian-Zadeh, F. Fotouhi, et al., Content-based image database system for epilepsy, *Computer Methods and Programs in Biomedicine*, 79:209 – 226, 2005.

[78] M.R. Siadat, H. Soltanian-Zadeh, F. Fotouhi, et al., Multimodality medical image database for temporal lobe epilepsy*, Medical Imaging 2003: Pacs and Integrated Medical Information Systems: Design and Evaluation*, 5033:487 – 498, 2003.

[79] "Siemens CAD", [online], Available: http://www.siemens.co.in/en/about_us/index/our_business_segments/sisl_healthcare/computer_aided_diagnosis.htm.

[80] "SPM5 - Statistical Parametric Mapping", [Online], Available: http://www.fil.ion.ucl.ac.uk/spm/software/spm5/.

[81] "Stroketool by DIS", [Online], Available: http://www.digitalimagesolutions.de/.

[82] "Summary of the HIPAA Privacy Rule", [Online], Available: http://www.hhs.gov/ocr/privacy/hipaa/understanding/summary/privacysummary.pdf.

[83] T. Tapiola, C. Pennanen, M. Tapiola, et al., MRI of hippocampus and entorhinal cortex in mild cognitive impairment: a follow-up study. *Neurobiol Aging*, 29:31 – 38, 2008.

[84] C. Testa, M.P. Laakso, F. Sabattoli, et al., A comparison between the accuracy of voxel-based morphometry and hippocampal volumetry in Alzheimer's disease. *J Magn Reson Imaging*, 19 (3):274 – 282, 2004.

[85] "The Whole Brain Atlas", [Online], Available: http://www.med.harvard.edu/AANLIB/home.html.

[86] P.J. Visser, F.R.J. Verhey, P.A.M. Hofman, et al., Medial temporal lobe atrophy predicts Alzheimer's disease in patients with minor cognitive impairment. *J Neurol Neurosurg Psychiatry*, 72:491 – 497, 2002.

[87] J.L. Whitwell, S.A. Przybelski, S.D. Weigand, et al., 3D maps from multiple MRI illustrate changing atrophy patterns as subjects progress from mild cognitive impairment to Alzheimer's disease. *Brain*, 130:1777 – 1786, 2007.

[88] J.L. Whitwell, M.M. Shiung, S.A. Przybelski, et al., MRI patterns of atrophy associated with progression to AD in amnestic mild cognitive impairment. *Neurology*, 70(7):512 – 520, 2008.

[89] W. Xu, A region growing algorithm for InSAR phase unwrapping. *IEEE Transactions on Geoscience and Remote Sensing*, 37(1):124 - 134, 1999.

[90] Y. Xu, C.R. Jack, P.C. O'Brien, et al., Usefulness of MRI measures of entorhinal cortex versus hippocampus in AD. *Neurology*, 54:1760 – 1767, 2000.

[91] A.H. Zhuang, D.J. Valentino, and A.W. Toga, Skull-stripping magnetic resonance brain images using a model-based level set. *NeuroImage*, 32:79 - 82, 2006.